UNIVERSITÀ DEGLI STUDI DI PADOVA

Dipartimento di Fisica e Astronomia "Galileo Galilei"

Master Degree in Astrophysics and Cosmology

Final Dissertation

Internal kinematics of stellar populations in M54 and in the Sagittarius dwarf galaxy

Thesis supervisor

Prof. Antonino Milone

Candidate

Marco Martorano

Academic Year 2020/2021

Acknowledgment

Abstract

Recent work discovered two distinct classes of Type I and Type II Globular Clusters (GCs). While Type I GCs are monometallic, the metallicity spread is a distinctive feature of Type II GCs, which indicates that these clusters have been much more massive at formation and retained the fast ejecta of SNe.

It has been suggested that Type II GCs are the remnants of much-more massive stellar systems, like dwarf galaxies that have been cannibalized by the interaction with the Milky Way. Hence, they may play an important role in the assembly of the Galactic Halo. Furthermore, they may increase the number of satellites orbiting the Galaxy and mitigate the missing satellite problem.

M 54 is considered the 'Rosetta Stone' to connect GCs and dwarf galaxies. Indeed, this massive Type II GC is located in the nucleus of the Sagittarius dwarf galaxy and provides the unique opportunity to constrain multiple populations in the galaxy and in the cluster.

The internal kinematics of stars in GCs may retain fossil information about the formation process of multiple populations and the connection with the host dwarf galaxy. However, while multiple populations in Type II GCs have been widely investigated by means of photometry and spectroscopy their internal motions are nearly unexplored. Indeed, it is challenging to derive accurate proper motions of stars within distant GCs.

In this work, I analyze multi-epoch images of M 54 collected by the Hubble Space Telescope through five filters. The exquisite multi-band photometry that I derived, allowed me to disentangle the main stellar populations in the Sagittarius galaxy and within M 54. Specifically, I identified a first generation 1G, composed of metal-poor stars with pristine helium abundance, a second generation composed of metal-poor stars enhanced in N and He, and a Fe-rich population made of N-rich He-rich stars. By comparing the position of stars at different epochs, I derive high-precision proper motions, that allowed me to measure, for the first time, the internal motions along the plane of the sky for stellar populations in the galaxy and in M 54.

I find that all stellar populations in the GC and the galaxy share the same mean motion. Moreover, I determined and investigated the velocity dispersion profiles of the stellar populations within M 54 and within the galaxy.

It results that stellar populations in M 54 and in the galaxy exhibit different velocity profiles, thus indicating that they had different origin. I provide the first analysis of the motions of the three main populations within M 54. On the radial axis the 1G, the 2G and the Fe-rich population show similar trends, while on the tangential axis the 1G deviates from the behaviour of both the 2G and the Fe-rich population. This finding suggests that stellar populations with different nitrogen abundances share similar motions regardless their metallicity. I discuss these results in the context of the formation scenarios of multiple populations.

Contents

1   Introduction

1.1   Globular Clusters in literature

Globular clusters (GCs) are systems containing up to millions of stars very tightly bound by gravity which gives these structures their characteristic spherical shape with a very high stellar density in the central region. They are believed to be among the oldest structures formed in the Universe with ages spanning from ten to more than thirteen billion years. They were also considered as the prototypical example of simple stellar populations characterized by stars with the same age, the same content of helium and metallicity and the same initial mass function. The metallicity changes from one GC to another and ranges from nearly solar (e.g. in NGC 6528) to [Fe/H]~ -2.4 (in M 15).

GCs are commonly found in the halo of galaxies but also the disk and the bulge are widely populated.

This classical view of GCs as simple populations has radically changed in the past few decades. Most recent discoveries on GCs rise from the space-based telescopes, that do not suffer the atmospheric perturbations, the improved detectors and the new manufacturing techniques in mirrors production. Furthermore, the new methods for data analysis are also responsible for the the beginning of a new era in GC studies.

All the new technologies provided new insights of GCs: recent photometric, astrometric and spectroscopic investigation highlight unexpected features of these intriguing objects that are now considered complex stellar populations.

Early evidence of 'chemical anomalies in GCs' come from spectroscopy of giant stars. In his review, Kraft (1979) provides overwhelming evidence that GCs are not as simple as thought: indeed, stars within the same cluster exhibit large spread of some light elements, including carbon, oxygen, nitrogen and sodium.

In addition to spectroscopy, photometry is another powerful tool to investigate the multiple-population phenomenon.

Major advances in GCs studies were provided by the synergy of the impressive Hubble Space Telescope (HST) data and the tools for data reduction by Jay Anderson and collaborators (Anderson & King, 2000; Anderson, 2003; Anderson et al., 2008) that will be deeply discussed in Section 2.3.

Recent works, based on high-precision *HST* photometry, reveal that the CMDs of GCs are not consistent with simple isochrones, but are composed of multiple sequences that can be followed continuously along different evolutionary phases and correspond to stellar populations with different chemical compositions. These finding shows that GCs are complex stellar systems whose CMDs differ from one cluster to another.

The *Chromosome Map* (Milone et al., 2015, Milone et al., 2017) is an efficient tool to identify and characterize multiple stellar populations in GCs. It is a photometric diagram sensitive to the abundance of light elements in GCs. It combines information from the HST filters F275W, F336W, F438W, F814W in the color $m_{F275W} - m_{F814W}$ and the pseudo-color
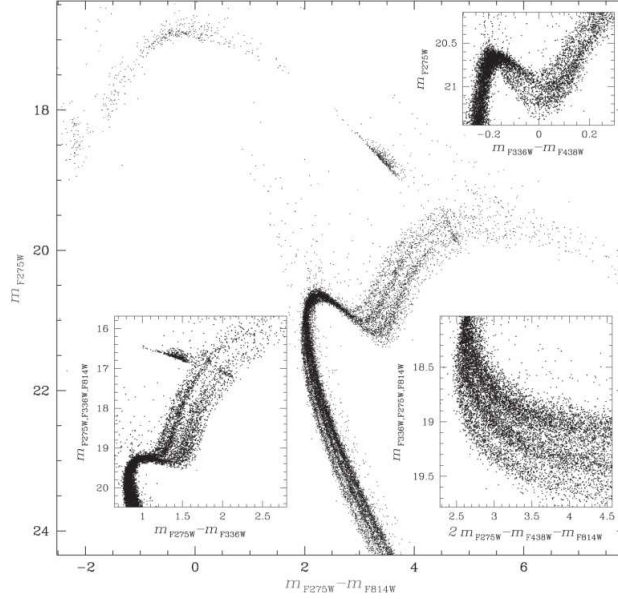
Figure 1: In this image is represented the CMD of the GC NGC 2808 as example of the impressive capabilities of the new methods for photometric studies. In addition it is possible to clearly see a splitted RGB which is due to different populations as a signature of the chemical inhomogeneities in the cluster. This image was taken from Milone et al. (2015).

$(m_{F275W} - m_{F336W}) - (m_{F336W} - m_{F438W})$.

The Chromosome Map, which will be widely used in this thesis to investigate stellar populations in M 54, is generally built for RGB, MS or AGB stars, separately. It exploits two distinct photometric diagrams that, in mono-metallic GCs, are mostly sensitive to the content of helium and nitrogen of stellar populations, namely the m_{F814W} vs. $m_{F275W} - m_{F814W}$ CMD and the m_{F814W} vs. $C_{F275W,F336W,F438W}$ pseudo-CMD. The first step to build the Chromosome Map consists in deriving the fiducial lines that mark the blue and red boundaries of each diagram. The blue boundary is derived by measuring the 4th percentile of the color distribution in small magnitude intervals and associating these values to the average magnitudes of stars in the same magnitude bin. The red fiducial is derived in the same way but by using the 96th percentile. The photometric diagrams are then rectified according to the equations (Milone et al., 2017)

$$\Delta_{F275W,F814W} = W_{F275W,F814W} \frac{(x - x_{red-fiducial})}{(x_{red-fiducial} - x_{blue-fiducial})} \tag{1}$$

$$\Delta_{F275W,F336W,F438W} = W_{F275W,F336W,F438W} \frac{(y_{red-fiducial} - y)}{(y_{red-fiducial} - y_{blue-fiducial})} \tag{2}$$

2

where $W_{F275W,F814W}$ represents the distance between the fiducial lines two magnitudes above the turn off, x is the color (or pseudo-color) of the star while $x_{red-fiducial}$ and $x_{blue-fiducial}$ are respectively the values of the red and blue fiducials at the same magnitude of the star.

The Chromosome Map is finally built plotting $\Delta_{F275W,F336W,F438W}$ versus $\Delta_{F275W,F814W}$.

The width of the Chromosome Map is indicative of the color and pseudo-color spread, measured two F814W mag above the MS turn off for RGB stars. The position of each star in the Chromosome Map depends on its chemical composition. Indeed, stars sharing the same chemical composition should lay on the same isochrone therefore are expected to be clustered around the origin of the Chromosome Map. On the contrary, the fact that some stars exhibit values of $\Delta_{F275W,F814W}$ and $\Delta_{F275W,F336W,F438W}$ that differ from zero is a signature of star-to-stars chemical variations.

Work based on the Chromosome Map reveal that all GCs host two main groups of first-generation (1G) stars that share the same chemical composition of field stars with similar metallicity and second-generation stars enhanced in He, N and Na and depleted in C and O (hereafter 2G stars).

The comparison between the colors of stellar populations identified on the Chromosome Map and simulated colors derived from grids of synthetic spectra with appropriate chemical composition, reveal that, in monometallic GCs, the $\Delta_{F275W,F814W}$ quantity is mostly affected by helium variations, whereas $\Delta_{F275W,F336W,F438W}$ mostly depends on the nitrogen content of multiple populations.

Intriguingly, the 1G sequence of the Chromosome Map is not consistent with a single isochrone but it exhibit intrinsic $\Delta_{F275W,F814W}$ spread. The physical reason of this spread is under debate. Helium variations and metallicity spread are the candidate responsible for the morphology of the 1G sequence in the Chromosome Map.

By collecting information from photometry, spectroscopy, and kinematics of 1G and 2G stars in large sample of GCs, astronomers have identified the main observational properties of multiple populations in GCs.

- **Discreteness**: the two populations 1G and 2G appear as distinct groups on the Chromosome Map of each GC analyzed.

- **Ubiquity**: all the GCs studied so far show the two generations in the Chromosome Map, therefore it is not a property linked to a single object but to the overall sample of galactic GCs.

- **Variety**: the properties shown by the two generations differ cluster by cluster (for example by number of stars per generation, number of sub-populations and extension of the Chromosome Map).

- **Two Classes**: according to Milone et al. (2017) in which a sample of 57 galactic GCs was studied, while the majority of clusters show a similar Chromosome Map
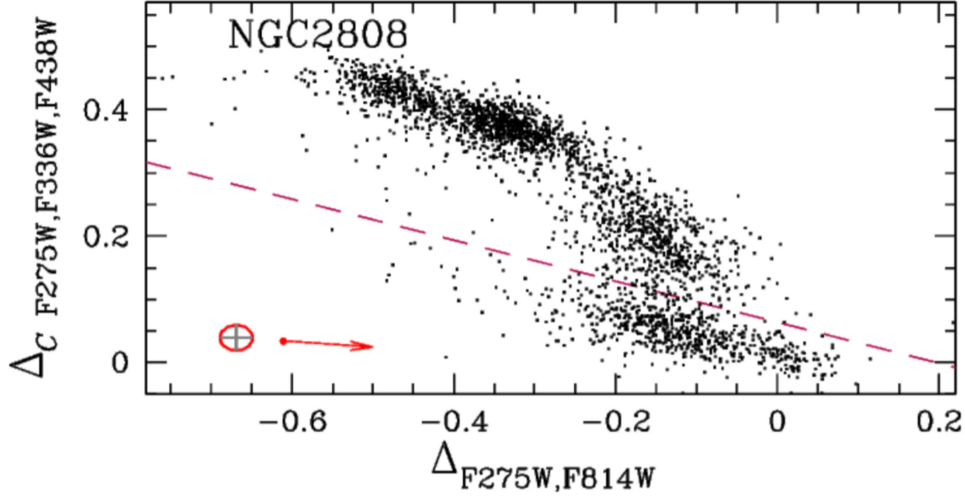
Figure 2: In this image is represented the chromosome map of the RGB of the GC NGC 2808 as an example. In first approximation it is possible to clearly distinguish the two populations: 1G below the line and 2G above. This image was taken from Milone et al. (2017).

characterized just by two distinct groups of stars, around 17% of them show a peculiar shape of the Chromosome Map with a group (possibly extended) that is separated by the two generations. Clusters showing this feature are referred to as *Type II* or *Anomalous* GCs. Examples of clusters member of this class are ωCen, $M54$, $M2$ and $NGC1851$ (figure 3). As summarized in Marino et al. (2021) Type II GCs hosts populations enhanced in the iron-group elements and in s-elements. In contrast to normal (Type I) GCs, the CMDs of the Anomalous ones show also multiple SGBs.

- **Dependence on cluster's mass**: the paper by Milone et al. (2018c) shows that the variations in the color $m_{F275W} - m_{F814W}$, used to build the Chromosome Map, correlate with the cluster's mass. On the same footing Lagioia et al. (2019) shows that also the variations in the pseudo-color $(m_{F275W} - m_{F336W}) - (m_{F336W} - m_{F438W})$, which is sensible to nitrogen variations, correlate with the mass of the cluster. Since the variations in the color and in the pseudo-color are extensions of the Chromosome Map and are the main descriptor of the multiple populations in the cluster, one can conclude that the multiple population phenomena in a cluster is strictly related to the mass of the cluster itself.

- **Maximum Helium enhancement**: in the paper Milone et al. (2018c) was also shown that there is a maximum value for the enhancement of helium which is $Y = 0.43$, with Y the helium fraction.

(a) Chromosome map of NGC 1851

(b) Chromosome map of NGC 5139 (ωCen)

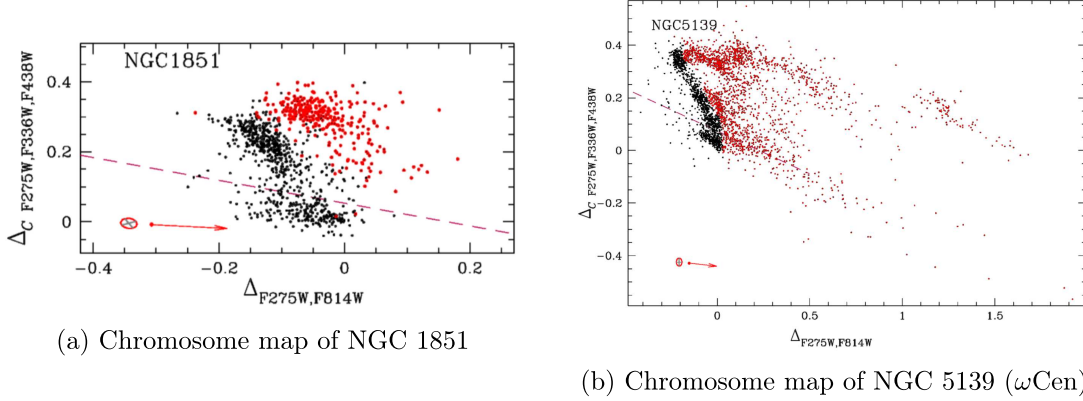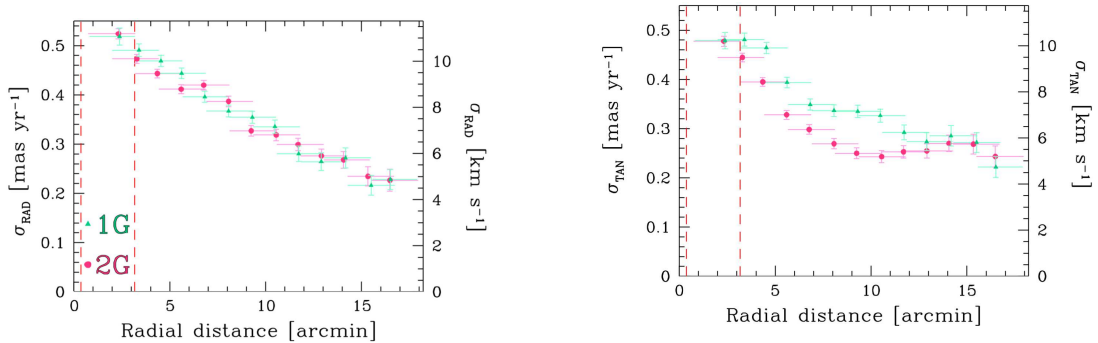Figure 3: These two pictures (from Milone et al., 2017) represent the Chromosome Map of two Anomalous GCs, namely NGC 1851 and ωCen. The red dots are considered by the authors as the members of the Anomalous populations

- **Dependence on GC's orbit**: Zennaro et al. (2019) stated that clusters with larger perigalactic radius host a larger fraction of 1G stars than those with a smaller perigalactic radius.

- **No dependence on stellar mass**: the study of Milone et al. (2019) analyzed the lower main sequence of the GC *NGC* 6752 showing that the population ratio of the three populations, clearly distinguishable in the lower main sequence of the cluster, was the same of that obtained considering the populations identified from the Chromosome Map of the RGB. Therefore the multiple populations are not a phenomena related to the stellar mass. Multiple populations are not a property just of RGB stars but are present in each part of the CMD.

- **More centrally concentrated 2G**: the analysis of the stellar density in GCs shows that in some GCs star belonging to the 2G tends to be more centrally concentrated than 1G stars. Example of clusters showing this peculiary are 47Tuc, ωCen, M3 and NGC 2808 (see Sollima et al., 2007; Bellini et al., 2009; Milone et al., 2012; Cordero et al., 2014; Dondoglio et al., 2021 and references therein).

- **Anisotropic motion of 2G stars**: as firstly showed in Milone et al. (2018a) which studied the velocity dispersion of the different populations in the GC 47 *Tuc* (see figure 4), and then extended by Cordoni et al. (2020b) and Cordoni et al. (2020c) studying also the rotational curves , in some galactic GCs stars belonging to the 2G show an anisotropic motion with a lower tangential-velocity dispersion than 1G stars.

These ten properties of multiple populations are used as reference to discriminate among

(a) Dispersion of velocities along the radial axis

(b) Dispersion of velocities along the tangential axis

Figure 4: These two pictures (from Milone et al., 2018a) represent the velocity dispersion along the radial (left picture) and tangential (right picture) axis of 1G (acqua triangles) and 2G (magenta circles) stars belonging to the GC 47Tuc. While the radial dispersion is comparable, the tangential is not.

the variety of scenarios which are used to describe the origin of multiple populations in GCs.

Scenarios are normally divided in two macro-families: *the multiple generation scenarios* which consider stars as born from multiple bursts, and *the simple stellar generation scenarios* in which the multiple populations are the results of exotic processes taking place during the star formation period.

- **Multiple Generations**

  1. *AGB scenario*: this scenario was proposed in the 80s and then improved by different authors (Ventura et al., 2001; D'Ercole et al., 2010; D'Antona et al., 2016). The 1G formed with a full initial mass function and after the first few million years the most massive stars explode as supernovae expelling the pristine material and halting the star formation. After $\simeq 30$Myrs AGB stars start to eject gas polluted with the ashes of the CNO cycle and s-process elements formed during the nucleosynthesis of the AGB phase. This material collects in the center of the cluster because of the strong gravity of the whole system. Contemporaneously the cluster, thanks to its large mass, is able to collect again some pristine gas which mixes with the polluted one in the cluster's center. Once the density of the gas become sufficiently high, a second burst occurs and 2G stars form. The cluster, that is still in its first millions years continuously expand loosing the outer stars (mostly 1G stars) into the galactic halo. This model is interesting because able to explain many features of multiple populations like the anti-correlation between oxygen and sodium, the concentration of 2G stars in the center of the cluster and also the anisotropic motion of this latter population. On the other

side it allows just for a maximum helium abundance in stars of Y=0.36 which do not agree with the value of 0.43 observed in Milone et al. (2018c).

2. *Fast Rotating Massive Star (FRMS) scenario*: this scenario was initially proposed by Decressin et al. (2007) and then further developed in Decressin (2010) and Krause et al. (2013). It consists in assuming the existence of fast rotating massive stars (with mass in the range 25-150$M_\odot$) which initially rotate with a speed near the break-up velocity. This fast rotation will bring matter from the convective core to the surface where mechanical winds cause a mass loss from the equator at low velocity. This causes the creation of a disk made of pristine gas polluted by the nuclear burning ashes of the FRMS. Gravitational instabilities in this disk lead to the formation of a second generation of stars which chemical composition agree with the observed one. At the end of its life the FRMS explodes as a supernovae clearing the cluster of all the pristine and polluted gas therefore halting the star formation process. Since FRMSs form (or migrate) in the center of the cluster, also the 2G will form there, thus this scenario is able to explain the central pile-up of 2G stars. In addition, if the gas expulsion acts on short timescales, it can affect the dynamical properties of the cluster by ejecting preferentially 1G stars. However, predictions allow for a maximum helium fraction between 0.60-0.70 which is much larger than the observed one. Interesting feature of this model is that since 2G stars born in the disks of massive 1G stars, 1G and 2G stars should share the same kinematics.

3. *Super-massive Stars scenario*: this scenario was studied in Denissenkov and Hartwick (2014) and assumes the second generation of stars born from the gas lost by a super-massive star. In particular the authors state that in order to explain the growing evidences of the presence of intermediate mass black holes in GCs, the anti-correlations in p-captures elements and the dynamical evolution of clusters that rises from simulations, super-massive stars (with mass larger than $10^4 M_\odot$) may formed both through runaway collisions of massive stars that sank to the cluster center as a result of dynamical friction, or via the direct monolithic collapse of the low-metallicity gas cloud from which the cluster formed. The super-massive star will be a short life star which may lost a large fraction of its mass because of stellar winds due to the exceeding of the Eddington limit. This gas is strongly polluted by the ashes of the nuclear burning taking place within the super-massive star. At the end of its life it will collapse and may form an intermediate mass black hole while the gas lost during all its life will mix with pristine gas and then will collapse to form the stars of the 2G. This scenario has the peculiarity of explaining the formation of intermediate mass black holes which presence is suggested by some authors in the middle of some GCs, even if there is not yet a direct observation of them within clusters. In the paper the authors remarks that if in young GCs super-massive stars formed from

the runaway collisions of massive stars that sank to the cluster centre through dynamical friction then this would explain why only GCs, but not dwarf galaxies, show the chemical anomalies named multiple populations. In fact, young dwarf galaxies were not compact enough for their first generation massive stars to sink to their center and merge there before exploding as supernovae.

4. *Massive Interacting Binaries (MIB) scenario*: this scenario (de Mink et al., 2009) considers the non negligible possibility that stars with mass larger than $20 M_\odot$ may form binary systems which, during their evolution, expel up to $10 M_\odot$ of both pristine and polluted material (the mass ejected is comparable to the envelope mass of the primary) enhanced in He, N, Na and Al and depleted in C and O. Since this gas is expelled with low velocity, it is retained within the potential well of the cluster and contributes to star formation. Authors showed that the polluted material injected this way in the cluster is much more than that injected for example in the AGB and rotating stars scenarios combined. Another peculiarity of this scenario is that it does not rule out the others but, on the contrary, the interaction of binaries lead to the formation of more intermediate mass stars which will evolve toward the AGB phase, and will also be responsible for the formation of new fast rotating stars which may loose polluted material because of mechanical winds.

- **Simple stellar generation**

  1. *Early-disc accretion in MIBs scenario*: the model envisioned by Bastian et al. (2013) considers a cluster which is forming with a classical initial mass function and the remnants of the pristine gas already ejected by the most massive stars evolved and exploded as supernovae. Massive interacting binaries (expected to be in the core) and spin stars will loose polluted material which is collected by the disk of forming pre-main sequence (PMS) low mass stars formed in the same generation but that have not yet reached the main sequence because of the slow evolution due to their low mass. Since massive binaries will form mostly in the cluster's core, just low mass PMS stars that during their formation pass near the core will accrete polluted material within their disk. Therefore, authors predict that polluted stars that nowadays are in the outer parts of the cluster should be preferentially on radially anisotropic orbits (they should have had a very elliptical orbit in order to pass near the cluster's center at their formation and now be in the outer part of the cluster) while those unenriched at large distance from the center should lay on almost circular orbits. Moreover, according to predictions, the polluted population is expected to rotate slower than the other but have aligned spin axes (Hénault-Brunet et al., 2015). According to this model there are no multiple bursts but a prolonged star formation.

  2. *Super-massive Stars scenario*: according to Gieles et al. (2018) GCs formed in

converging gas flows and accumulate low-angular momentum gas, which accrete onto protostars (figure 5). This leads to an adiabatic contraction of the cluster and an increase of the stellar collision rate. If the stellar density in the core of the cluster was sufficiently high, may a super-massive star (with mass larger than $10^3 M_\odot$) formed before the two-body relaxation halts the core's contraction. This condition is met if the number of stars is larger than 10^6 and the gas accretion rate is of the order of $10^5 M_\odot/Myr$. The strong super-massive star's winds mixes with the in-flowing pristine gas and, because of continuous rejuvenation, the amount of processed material freed by the SMS can be one order of magnitude higher than its own mass. This model predicts that polluted stars would have more radially anisotropic orbits since initially they were more centrally concentrated.
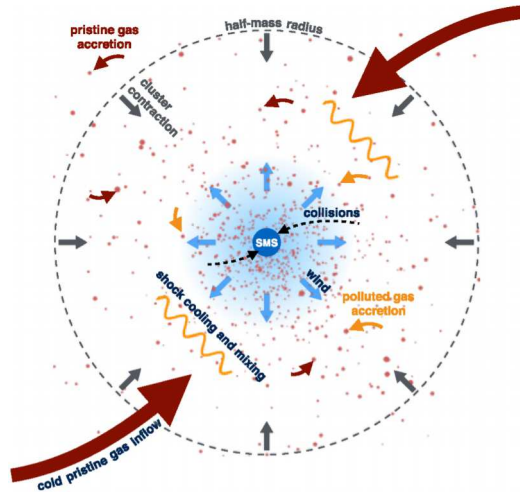

Figure 5: This image from Gieles et al. (2018) is the graphical representation of how the super-massive stars scenario predicts the infalling and processing of gas by the super-massive star.

All the scenarios relative to a multiple burst are characterized by the so called *Mass Budget Problem*. It consists in the fact that the 2G today appears much more massive than the 1G but since according to these models 2G stars formed from polluted materials of 1G massive stars, then the 1G at its formation should have been much more massive than what inferred from its present mass distribution. For example, according to the AGB scenario, the original mass of the 1G should have been at least ten times larger than what predicted from its present day mass function. This problem instead does not affect the super-massive stars scenario proposed by Gieles et al. (2018) since the super-massive star is expected to process a total amount of mass even larger than ten times its own mass.

As I tried to summarize above, each scenario able to explain multiple populations has some drawbacks and up to now the scientific community is still divided on the most reliable one. However, each one is characterized by different peculiarities which explain some observational properties that can be studied in order to shade light on the formation mechanism of multiple populations. These observational evidences are mostly related to the chemical abundances and the population ratios while some other are related to the stellar density and to the kinematics of the system.

This work will try to investigate some of them on a particular target: the GC M 54 and the nuclear region of the Sagittarius dwarf galaxy.

1.2 M54 in literature

One of the most interesting properties related to multiple populations and listed before is the existence of two macro families of clusters: *Type I* and *Type II* (or *Anomalous*).

As briefly discussed in section 1.1 Type I GCs are the most common and are characterized by two distinct groups in the Chromosome Map, referred to as 1G and 2G which differ by the helium, carbon, oxygen and nitrogen fractions. On the other hand, Type II GCs are referred to as Anomalous because they are just the 17% of the whole and are characterized by an extended 2G which is possibly associated to many sub-populations. According to different papers which studied those clusters from a spectroscopic point of view (i.e. Marino et al., 2015; Marino et al., 2021), the stars composing these systems do not show just a spread in light elements but also in s-elements and in the iron group elements. This feature is sort of exotic since, for what known up to now, s-elements are produced just by evolved stars or cosmic rays spallation while elements of the iron group are expected to be produced just by supernovae.

The formation of multiple populations with a spread in metallicity (and in particular in the iron content) cannot be easily explained with the models discussed above which are developed to explain the spread in light elements. Some models, like the AGB one, are able also to explain the spread of s-elements which are produced during the AGB phase of intermediate mass stars of the 1G but they still are not able to explain a spread in the iron group elements. For what is known so far, metals are produced just during the explosion of supernovae but the gas ejected from supernovae have speeds larger than the escape velocity of the forming cluster and tends to escape it. In order to retain the gas ejected by supernovae the mass of the system should have been larger than that of a GC, like that of a dwarf galaxy.

These kind of observations lead to the speculation that Type II GCs may be the relics of dwarf galaxies cannibalized by the Milky way. In this scenario each Anomalous GC would represent an old merge and therefore this would alleviate the missing satellites problem providing new counts in the missing dwarf satellites population of the Milky Way. Indeed these are not the only observational evidences pointing in this direction: ωCentauri (ωCen) is cataloged in Milone et al. (2017) as a Type II GC showing internal variations in metallicity

and, supporting the hypothesis speculated above, it is believed to be the nucleus of a disrupted dwarf (Bekki & Freeman, 2003). Moreover, other studies (i.e. R. A. Ibata et al., 2019) show evidences of the existence of tidal debris correlated to ωCen as if the stars of its hosting dwarf, less gravitationally bounded than those of the cluster, mixed with the Milky Way's stars. Another evidence is related to stellar streams which nowadays are widely accepted as the signature of the tidal interactions of systems merging (or merged) with the Milky way: as shown by Milone et al. (2020) half of the known Type II GCs appear clustered in a distinct region of the integral of motions space, suggesting a common progenitor galaxy.

Another Type II GC that shows features which may confirm the speculation that Anomalous GCs are the remnants of past mergers with dwarf galaxies is NGC 1851. It is characterized by having a surrounding low density halo (Olszewski et al., 2009), whose chemistry was deeply studied by Marino et al. (2014) and is compatible with the s-poor group observed in this cluster. The absence of s-rich stars in this halo can be explained in two ways: or the cluster is loosing preferentially s-poor stars in the field, or the surrounding halo is the remnant of stars composing a yet disrupted dwarf galaxy which in the past hosted NGC 1851 but that then was absorbed by the Milky Way leaving just the cluster and some stars trapped by its gravitational well which now constitutes its halo.

Obviously as suggested in Marino et al. (2015) there are also some evidences that seems to undermine the hypothesis that Anomalous GCs are the remnants of dwarf galaxies merged with the Milky Way, for example the $[Fe/H]$ kernel-density distributions of dwarf galaxies shows a slow increase from lowest abundance to the peak while, on the contrary, Anomalous GCs like ωCen show a sharp rise to the metal-poorer peak. Another evidence in contrast to the hypothesis is that while Type II GCs show the typical anti-correlations pattern among light-element abundances, this is not present in dwarf galaxies.

To sum up, studying Type II GCs would be of fundamental relevance to understand whether they originated in a dwarf galaxy environment and therefore are the remnants of old mergers of these structures with our galaxy, or if their spread in metallicity and s-elements have some other exotic explanation.

An intriguing possibility is that suggested by Bekki & Yong (2012) which tries to explain the light-elements anti-correlations as the results of mergers among different clusters. This sounds exotic and fascinating mostly because, if the formed cluster is not yet relaxed, may some kinematical features of the initial clusters are still present and measurable. However as a drawback of this model spectroscopic evidences come in place: assuming true the hypothesis that Type II GCs formed as a merger of different clusters, the expected chemical composition of the newly formed Type II GC should be very heterogeneous while observations shows that the populations within Type II GCs are quite homogeneous.

The origin and evolution of Type II GCs are still strongly debated and different studies are carried on the topic.

However, despite all, one of the most intriguing target to investigate the possibility that Type II GCs are the relics of dwarf galaxies merged with the Milky Way and, more

in general, to try to shed light on the formation mechanisms of multiple populations in Anomalous GCs, is M 54.

M 54 (known also with the name of NGC 6715) was firstly discovered by Charles Messier in 1778 and initially cataloged by him as a comet-like object. Further studies identified it as a GC and just more recently, in the 20th century, it was acknowledged as the first GC ever discovered outside the Milky Way. In particular R. A. Ibata et al. (1994) discovered the presence of a dwarf galaxy named for the first time *Sagittarius dwarf galaxy* (Sgr) which center hosts the GC M 54. If this GC really is the nucleus of the dwarf spheroidal or if it migrated toward the center of the system is still debated even if the scientific community seems more convinced of this latter possibility. According to Monaco et al. (2005) it seems that stars of the dwarf spheroidal would have nucleated even without M 54, supporting the hypothesis that M 54 migrated toward the center probably because of dynamical friction.

While M 54 was identified already in the 18th century, the Sagittarius dwarf was detected just recently because of its current position. Although M 54 has coordinates RA=$18d\,55m\,03s$ and DEC=$30:28:41.9°$ thus is clearly visible with modern instrumentation below the bulge of our galaxy, the Sagittarius dwarf extends for many degrees along the declination axis being partially covered by the regions characterized by huge absorption near the Milky Way's bulge. This made its identification more difficult and explains why it was discovered just thirty years ago.

The system $M\,54+Sgr$ is widely studied in literature also because the Sagittarius dwarf is currently merging with the Milky Way (R. A. Ibata et al., 2001) as showed by the Sloan Digital Sky Survey data. The tidal arms created by this on going merge encircle all the Milky Way. Still these days new GCs associated to the Sagittarius dwarf are continuously discovered: according to Minniti et al. (2021) (which study is based on data from the VISTA survey[1]) up to now are known 29 GCs associated to the Sagittarius dwarf spheroidal showing that this dwarf galaxy hosts a very rich population of GCs.

From the photometric point of view different authors investigated this system, i.e. Sarajedini and Layden (1995) highlight the presence of a stellar population related to M 54 with a metallicity of $[Fe/H] = -1.79 \pm 0.08$ and another population associated to the Sagittarius dwarf with a metallicity $[Fe/H] = -0.52 \pm 0.09$. According to the authors both the populations may have a spread in metallicity. This was a conclusion particularly exotic in 1995 for what concern a GC which was expected to be chemically coeval. Unfortunately the quality of the photometry used in pioneering works on $M\,54+Sgr$ was not sufficient to clearly split the populations within this peculiar system.

A huge step forward in the photometric description of the system was done by Siegel et al. (2007) using the visual filters F606W and F814W of the Hubble Space Telescope (HST). These are the first observations of M 54 carried by Hubble with the ACS camera which grant an impressive photometric accuracy. Thanks to the new data-set the authors were able to

---

[1]Website of the VISTA survey https://www.eso.org/sci/facilities/paranal/instruments/vircam.html

obtain the photometry of nearly 390,000 sources from which they selected just the 60,000 with the most star-like profile in order to minimize the contamination of external sources or the poorly detected ones. From the resulting CMD (see figure 6) Siegel and collaborators were able to identify five different populations: a 13Gyr one with $[Fe/H] = -1.8$ associated with both M 54 and an old component of the Sgr dwarf; two intermediate populations with age 4 and 6Gyr with $[Fe/H] = -0.5$; a young population (2.3Gyr) with $[Fe/H] = -0.1$ and a very young population (0.1-0.8Gyr) with $[Fe/H] = +0.6$. Although the RGBs and the SGBs of these populations are quite well separated, the main sequences are almost completely overlapped using these HST's filters. Moreover the sequences crosses each other at the beginning of the RGB making difficult a clear separation of the populations in this region. Despite the difficulties this paper provide a deep photometric insight of this system.

More recently, thanks to new HST observations of this peculiar system, the study of Milone (2016) focused more on the analysis of multiple populations within M 54. Combining the observations used by Siegel et al. (2007) in the filter F814W and the new observations in the HST's UVIS filters F275W, F336W and F438W the author was able to build the diagram dubbed *Chromosome Map* (see section 1.1) for stars of the system belonging to the RGBs. Contrary to the majority of GCs, M 54 showed a Chromosome Map with two sequences of stars in close analogy with that observed in Anomalous GCs; he noticed also that each sequence exhibits distinct clumps demonstrating therefore that both the normal and the anomalous group host sub-populations characterized by variations in helium and light-elements.

In addition to the discussion carried on the multiple populations within M 54, this paper also showed the impressive ability of the combination of UV and optical filters in the separation of the intermediate and young populations related to the galaxy from the old ones related to both M 54 and the Sgr dwarf spheroidal.

In parallel to the photometric studies discussed above different authors investigated the properties of the system from both a spectroscopic and a kinematic point of view.

For what concern the spectroscopic studies, among all the papers in literature, Carretta et al. (2010) is a representative one. The authors derived the chemical composition of RGB stars both in the old and young populations which Siegel et al. (2007) relate respectively to the cluster and to the Sagittarius dwarf. They analyzed the abundances of O, Na, Mg, Al, Si, of $\alpha-$elements, and of Fe$-$peak elements. The results show that the majority of stars in the old population have $[Fe/H] \simeq -1.6$ with an intrinsic dispersion of $\simeq 0.19dex$ manifesting itself as a long tail toward higher metallicities. This metallicity spread is compatible with that observed in dwarf galaxies, therefore these results support the idea that M 54 can be identified as a nuclear star cluster. The Sagittarius nucleus (those populations which are younger than that constituting M 54) shows a metallicity of $[Fe/H] \simeq -0.62$ which is similar to the value found for the intermediate age population in the photometric studies.

Further studies were carried over the chemical composition of M 54 and more in general on a large sample of GCs in order to investigate the differences among Type I and Type II GCs and a summary can be found in Marino et al. (2019).
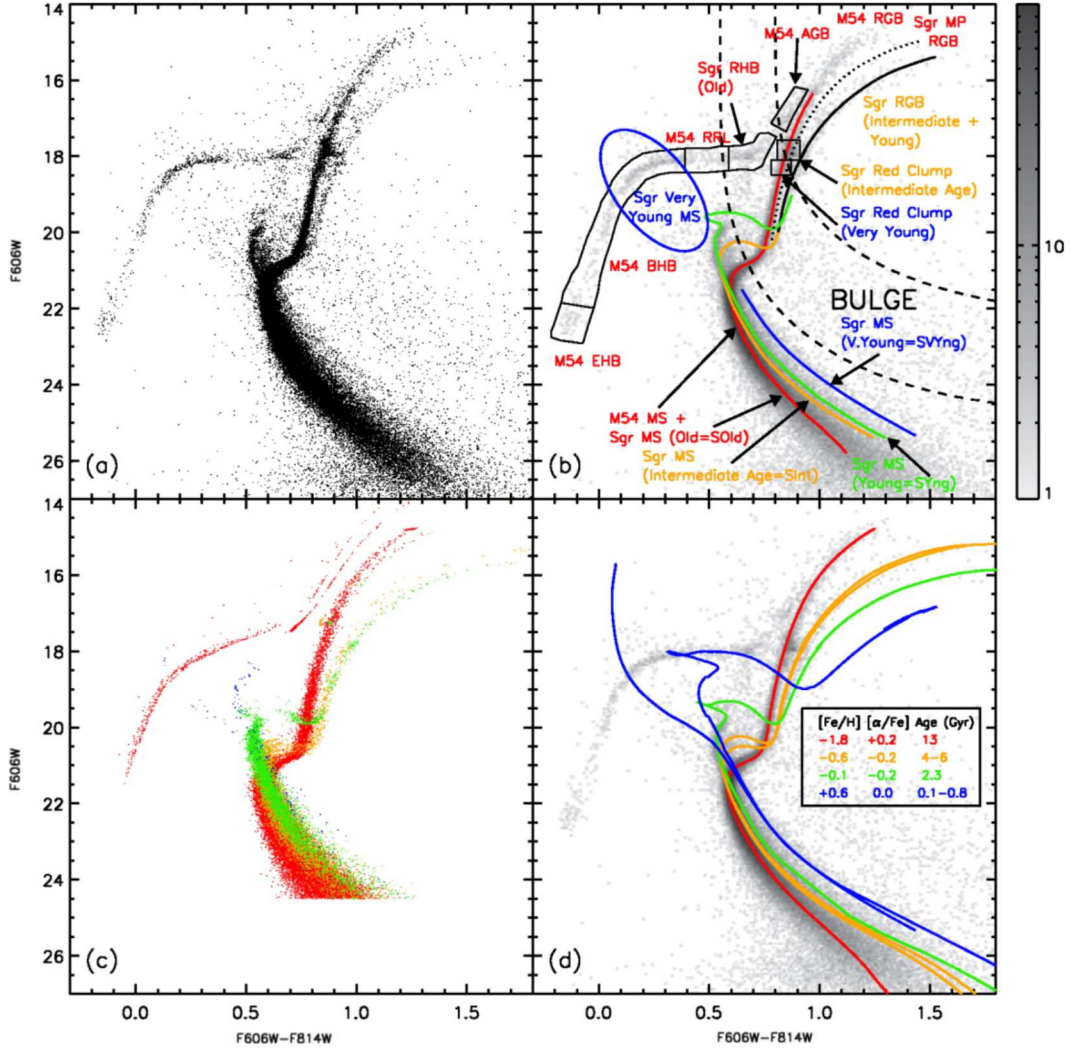
Figure 6: This picture represents the CMD obtained by Siegel and collaborators with highlighted the different populations identified by the authors. Top left is the CMD of the selected star, top right is the equivalent Hess diagram, bottom left is the CMD overlapped with simulated stars to infer the parameters of the populations and bottom right is the Hess diagram overlapped with the theoretical isochrones inferred in the study. This image was taken from Siegel et al. (2007).

M 54 is deeply studied also from a kinematical point of view. In particular, since nowadays is widely accepted that it is related to the Sagittarius dwarf galaxy, it is considered one of the most intriguing targets to search intermediate mass black holes. Different studies
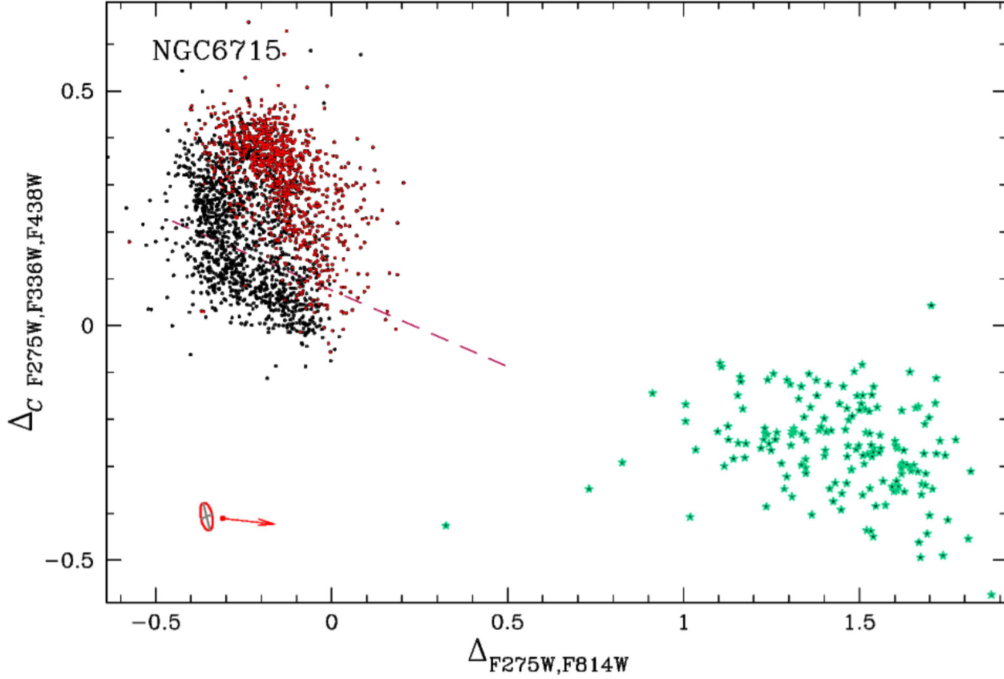
Figure 7: Chromosome Map of M 54 (black dots are the classical 1G and 2G while red dots constitute the anomalous population) and the young populations associated to Sagittarius (acqua stars). This Chromosome Map was taken from the paper Milone et al. (2017).

were carried out to investigate this possibility (i.e. Noyola et al., 2009; R. Ibata et al., 2009) suggesting the presence of an intermediate mass black hole with a mass $M \simeq 10^4 M_\odot$. In each case the results were obtained fitting King's models to the density profile and the velocity dispersion profile in the central regions of the cluster. The high accuracy required to study the velocity dispersion profile was obtained from radial velocity measurements. Although the presence of an IMBH is an exotic and fascinating possibility, R. Ibata et al. (2009) highlight that, although it is the most reliable, it is not the only possibility to explain the the cusps in the density and velocity profiles (i.e. a cold dark matter cusp, a population of massive stellar remnants or peculiar stellar kinematics). These author also highlight with a Jeans analysis that the young populations associated to the Sagittarius nucleus reveals a tangential anisotropy probably relic of the formation of the system.

The kinematics of this system was also studied in Alfaro-Cuello et al. (2020) where the authors used radial velocities of more than 6000 stars to investigate how the different populations in the system behave one respect the other. They found that the velocity dispersion of the old population follows a plummer profile with a central velocity dispersion of $\sigma_0 = 15.30 \pm 0.54 km\,s^{-1}$. According to their study the system is not characterized by

4 populations as suggested by Siegel et al. (2007) but 3: the old one, an intermediate one with an age of $4.28 \pm 0.09 Gyr$ and [Fe/H]$=-0.29 \pm 0.01$ and a young population with age $2.16 \pm 0.03 Gyr$ and [Fe/H]$=-0.04 \pm 0.01$ (these values come from Alfaro-Cuello et al. (2019) which is the first paper of an on going work). Respectively the central velocity dispersion of these two are $\sigma_{0_{intermediate}} = 15.21 \pm 0.89 km\,s^{-1}$ and $\sigma_{0_{young}} = 12.56 \pm 0.72 km\,s^{-1}$ and intriguingly none of these two has a trend compatible with a plummer profile.

This thesis is particularly focused on the kinematics of stars within the system $M\,54 + Sgr$ not aiming to the identification of an IMBH but to study the kinematical properties of the populations in the system, similarly to what done with radial velocities in Alfaro-Cuello et al. (2020), but with a strong effort on the sub-populations within M 54 which have never been studied from a kinematical point of view using proper motions. Indeed, the identifications of kinematical properties among different populations within M 54 may allow to shed light on the formation mechanisms of the populations themselves. Moreover, similarities between sub-populations in M 54 and in the younger populations related to the Sagittarius nucleus may suggest a new link between Type II GCs and the environment of dwarf galaxies opening the way to future studies.

Aiming this I will re-analyze the HST's data-set of multi-band and multi-epoch images taken in 2006, 2013 and 2014 and already used in the photometric studies described above. Although in this work are not used new data, I will recover the proper motion of the stars in the system which is a feature yet to be unveiled. Focusing on the velocity dispersion profiles this work will tackle the relations among different populations in the system from a completely new point of view.

As said before this system was never studied from the point of view of proper motions thus any result that I will obtain will be something completely new. Similar studies were carried on $47\,Tuc$ which however is a Type I GC and it is not associated with a dwarf galaxy as M 54, therefore the kinematical properties may be different. Assuming however that 1G and 2G stars behave as those in $47\,Tuc$, I expect to obtain results similar to those of Milone et al. (2018a): 2G stars should strongly deviate from isotropy with the maximum deviation at a distance from the center of about two half-light radii while 1G should not show deviations from isotropy. Marino et al. (2014) analyzed the velocity dispersion of the cluster $NGC\,1851$ which, as already discussed previously, is a Type II GC characterized by the presence of a spherical halo. This work was based on the radial velocities of stars therefore the number of stars used was much smaller than what can be in principle obtained from HST, however the authors were able to show that the velocity dispersion of the halo's stars follow the same profile of the cluster's member. In the assumption that the halo's stars are members of the host galaxy already disrupted, I expect similar behaviours for the young populations associated to the Sagittarius dwarf spheroidal. In any case, as studied in Alfaro-Cuello et al. (2020), stars belonging to the cluster should show a gradient in the velocity dispersion with the distance from the center of the cluster compatible with a Plummer profile (Plummer, 1911) while stars in the young populations, if really belong to the galaxy, should not be characterized by this strong gradient but by an almost constant

trend typical of large structures.

Obviously, if the populations are all mixed and the system is fully relaxed it may be that no differences among populations light up. This is quite common in old structures like GCs. However, $M\,54 + Sgr$ is characterized by the presence also of young populations which possibly are not still completely relaxed.

1.3   Thesis layout

Everything reported here above is a summary of the present day knowledge of GCs and of the point of interests of $M\,54 + Sgr$ system which is the target investigated in this work.

As shown by different authors this peculiar system is the prototypical example of Type II GCs and is the only one so far known to be certainly related to the nuclear environment of a dwarf galaxy, being therefore the ideal target to look for properties in common between the populations related to the Sagittarius nucleus and those in the GC $M\,54$.

This work aims to unveil some new kinematical properties of this system and of its populations in order to search for evidences which might explain its formation and its evolutionary history shading light not only on the formation mechanisms of multiple populations within GCs, but also on those characterized by the spread in metallicity which is a signature of Type II GCs. The possibility of comparing kinematical properties associated to the young populations related to the dwarf galaxy with those related to the sub-populations in $M\,54$ is an almost unique feature of this system worth to be investigated.

The thesis is organized as follow: section 2 contains a review of the instrumentation used to collect the data (sec. 2.1) and a detailed explanation of how I retrieved images (sec. 2.2), reduce them (sec. 2.3) and build up the photometric (sec. 2.4) and the astrometric (sec. 2.5 and 2.6) catalogs, then in section 3 I explain how I have selected the different populations from the photometric catalog and the methodologies adopted to study the internal kinematics of the different populations. Finally in section 4 are reported all the results obtained in this thesis with a discussion on their implications.

2 Data Reduction

2.1 Instrumentation

Studying the photometric and astrometric properties of a GC at great distance as M 54 (26.5kpc according to Harris, 1996, 2010 edition), requires very accurate multi-band and multi-epoch photometry over a long temporal baseline. With this purpose data for this project are taken from the Mikulski Archive[2] where the Hubble Space Telescope (HST) data are stored.

The great resolution of HST combined with its peculiarity of being in orbit and therefore sensitive also to ultra-violet (UV) light (which is not easily detectable from ground-based detectors because of the huge atmospheric absorption) makes HST the best instrument for the kind of work that will be carried out in this thesis.

Data used for this project are obtained from the Wide Field Camera 3 (WFC3) and the Advanced Camera for survey (ACS). While the first one is used to gather data in the UV-visible band since works in the range $(2000-11000)$Å, the latter provides the data in the visible and near-infrared band.

Both the ACS camera in the Wide Field Channel and the WFC3 camera are made of two CCDs each with 2048x4096 pixels allowing an angular resolution of 0.04 $arcsec/pixel$. This impressive resolution results fundamental in the analysis of the GCs allowing for the separation of many different sources therefore opening the way for the study of crowded regions like clusters' cores. In addition, the great angular resolution allows the determination of stars' positions with an unprecedented accuracy therefore permitting, through the study of multi-epoch images, the investigation of stellar proper motions. Indeed, another great advantage of using HST is that the ACS camera is active since 2002 while the WFC3 from 2009 therefore the two camera together provided an impressive amount of data during their lives and they are still operative collecting new images each orbit. This means that the temporal baseline over which HST's images are taken is enlarging continuously.

Since part of the work consists in acquiring the knowledge necessary to reduce HST data, I will not work with pre-reduced data or already compiled catalogs but starting from raw data I will realize a new catalogue which will be publicly released to the scientific community in the near future.

2.2 HST images retrieval

From the Mikulski Archive I downloaded the images of M 54 and the surrounding two arcminutes in fits format collected by HST with the UVIS-CENTER aperture in three different epochs: for visual wide filters F606W and F814W in 2006 while for the UVIS wide filters

---

[2]Based on observations made with the NASA/ESA Hubble Space Telescope, obtained from the data archive at the Space Telescope Science Institute. STScI is operated by the Association of Universities for Research in Astronomy, Inc. under NASA contract NAS 5-26555.

F275W, F336W and F438W in 2013 and 2014. A summary of the downloaded images is reported in Table 1.

An important effect to keep into account when working with HST images is the Charge Transfer Efficiency (CTE). This effect describes the loss of electrons during the transfer between the pixels of the CCD in the readout process and it arises mostly when a detector ages. It causes the point-spread function (PSF) describing the star to assume a drop shape. HST's cameras are strongly affected by CTE reduction mostly because the detectors ages much faster than their similar on ground: in space, in fact, the huge amount of cosmic rays and energetic particles, which on ground are mostly blocked by the Earth's magnetic field and atmosphere, deteriorate the detectors causing a reduction of the CTE and therefore worsening the image quality and the data usability. However, all the images collected from the Mikulski archive are already corrected for CTE by the team of the Space Telescope Science Institute operated by the Association of Universities for Research in Astronomy.

The files .fits downloaded are composed of two frames (one per CCDs) and counts per pixels are saved as float variables making the file quite heavy. Without loosing of generality, the images within the same file are stacked together and the counts are rounded to the nearest integer. This procedure is carried out with the routines *flt2wj2_wfc3uv.F* and *flt2wj2_acswfc.F* (depending if the image was taken with the ACS or the WFC3 camera) written by J. Anderson[3] in FORTRAN language. They allow to obtain a unique file containing the information of both the CCDs in a single frame with a strong reduction of the memory required. Indeed, the possibility of working with integers instead of floats strongly reduces the computational power required for the data analysis without affecting the data resolution since the relative errors in using integers or floats when working with values of many hundreds or even thousands (which are common values of counts per pixel) is substantially negligible.

Images obtained this way are surveyed by eye to search for interesting features like unknown clusters in the background (i.e. that found by Milone et al., 2018b). Unfortunately this survey brings to no new discoveries. However, this check was everything but useless since highlighted the presence of a lot of cosmic rays (CRs) which populate all the images in all the filters. They manifests themselves mostly as bright straight lines of few tens of pixels, but they can have different shapes which may be confused with stars. As a consequence a way of separating stellar candidates from noise is needed. This issue can be partially solved through the point-spread function (PSF) fitting.

2.3   PSF fitting and star selection

Once the different CCDs' frames are stacked together and opportunely organized by filter, I can go further to identify and extract the stellar sources from each image. This can be achieved with the evolution of the code img2psf written by J.Anderson and described in

---

[3]see its website at the Space Telescope Science Institute https://www.stsci.edu/stsci-research/research-directory/jay-anderson

Table 1: Parameters of the HST's images used as data-set for this work. In this table are reported: "EPOCH" is a name used to identify images taken in the same year; "DATE" is the date at which the image was taken; "FILTER" is the filter used by HST to take the image; "EXPOSURE" is the exposure time used; "#IMAGES" reports the number of images taken that day in that filter and with that exposure;. Visible filters F814W and F606W were taken during the GO 10775, while UVIS filters F275W, F336W and F438W were part of the GO 13297. These are all the images in the UVIS-CENTER aperture which are available on the Mikulski Archive.

EPOCH	DATE	FILTER	EXPOSURE	#IMAGES
E0	25/05/2006	F606W	340s	10
	25/05/2006	F606W	30s	2
	25/05/2006	F814W	340s	10
	25/05/2006	F814W	30s	2
E1	05/09/2013	F438W	190s	1
	05/09/2013	F336W	475s	1
	05/09/2013	F275W	1920s	1
	06/09/2013	F438W	190s	1
	06/09/2013	F336W	475s	1
	06/09/2013	F275W	1916s	1
	07/09/2013	F438W	190s	1
	07/09/2013	F336W	475s	1
	07/09/2013	F275W	1920s	1
E2	29/06/2014	F438W	170s	2
	29/06/2014	F336W	433s	2
	29/06/2014	F275W	1755s	2
	03/07/2014	F438W	170s	1
	03/07/2014	F336W	433s	1
	03/07/2014	F275W	1751s	1

Anderson & King (2000), Anderson (2003), and Anderson et al. (2008) which was created for the WFC2 camera and then modified and extended to both the ACS and the WFC3 (and is going to be adapted also for cameras on board of the James Webb Space Telescope).

Conceptually the idea consists in splitting the image in sub-sectors and for each sub-sector find the best PSF that better represents the stars there. While splitting the image allows to cancel out CCD's inhomogeneities, the determination of the best PSF allows to obtain sub-pixel resolution for the stars' position. If no inhomogeneities or any kind of disturbances would be present, then the star's profile would be a Gaussian one with up to 40% of the flux in the central pixel and up to 8% in the four adjacent, but since CCDs are not perfect and between the source and the detector many different things can distort the light, the profile could not be perfectly Gaussian. The method developed by Anderson and collaborators keeps also this into account allowing for any kind of shape for the PSF profile. Authors claim to have an accidental error of measurement on the star's position using this method for the PSF determination of about 0.02 pixel which grant an impressive resolution.

The determination of the PSF profile is everything but easy since drastically different PSF profiles are able to describe the same integrated flux on adjacent pixels. This problem arises mostly in under-sampled images which however are not the case of this work. Nevertheless fitting the PSF profile at its best is fundamental when the aim is getting precise astrometry especially when systems are far away and stars move of a fraction of pixel per year.

The PSF may change star by star also because of the thermal expansion and contraction of HST during its orbit or changes in the focus. Moreover, as the authors discuss recalling the paper by Lauer (1999), the PSF strongly depends on the discrete nature of the image: CCD's pixels have different sensitivity thus the counts (and consequently also the shape of the PSF) changes depending on the position of the star within the pixel; in addition there is also a tendency for photo-electrons to diffuse out of the pixel in the nearby ones when the pixel is almost saturated. To solve this puzzle the authors define an *effective PSF* which is a continuous function that exactly describe the fraction of a star's light that should fall in each pixel depending on where the star lies with respect to the center of the pixel itself.

The author's idea is to initially select some reference stars which are isolated and sufficiently bright to be easily detected. Then their code selects a grid of 5x5 pixels around each of these stars and samples the effective PSF in each pixel starting from a reference PSF model. Since each sampled value is independent by the others, in the end they will have 25 samples of the effective PSF for each star of the N analyzed. These samples are used to get a new PSF which is much more reliable than the starting model since based on the real measurements.

The procedure is repeated iteratively using as starting PSF model the effective PSF obtained with the previous cycle. This iterative procedure grant good accuracy in the PSF determination.

The code used in this work allows for the selection of some parameters:

- HMIN: this parameter allows to set a minimum distance (in pixels) that must be present between a reference star, that will be used for the effective PSF determination, and its neighborhoods. For this work I set HMIN to 13 pixels which is a common

value.

- FMIN: this parameter represents the minimum flux (i.e. counts) that a star must have to be considered as a good reference for the effective PSF determination. In this work I set it to 5000.

- PMAX: with this parameter one can select the maximum number of counts that a pixel can have in order to consider that star as a good one. It allows you to get rid of saturated stars. I set it to 54900 which is a reference value for HST ACS and WFC3 cameras.

- QMAX: when the code compare the flux distribution of the star with the predicted one, it is possible to compare the values obtaining a quality parameter (hereafter *Qfit*) which tells the goodness of the fit for those stars. In other words I expect stars-like sources having a PSF similar to the model while all the noisy sources such as CRs or background quasars, will have a PSF different from the expected one. Therefore, the *Qfit* is a parameter that can be used to separate very good candidate stars from noisy sources or stars that are not well fitted such as faint stars which are strongly affected by noise. This parameter should be changed image by image to include more or less reference stars according to what permitted by the quality of the image, but after many trials I noticed that in the data at my disposal there is a sufficiently high number of good stars in each image to set the *QMAX* value to 0.2 for all the images in my data-set. An higher value would have allowed for a larger sample but would have also included some noisy sources which would have spoiled the PSF, while a lower one would have strongly cut the number of samples over which computing the effective PSF therefore decreasing the accuracy.

- NSIDES: this parameter sets the number of sub frames in which the image is divided in order to get a PSF for each sub-frame, getting this way rid of systematical errors due mostly to inhomogeneities in the CCDs. In my work I set it to one which means that the image is not divided in sub-frames. I was substantially forced to this choice since the good targets of the image are not uniformly distributed (i.e. I don't have good stars to use as reference in the center of the image because being the cluster very crowded there is not the minimum distance HMIN between sources required for the selection of references). As a consequence I cannot get rid of the inhomogeneities of the CCDs. This won't be a major issue for this work since this inhomogeneities become relevant mostly for faint sources which are not the main target of this project.

Exist two different ways to get photometry starting from HST images: the first one consists in reducing each image singularly while the second consists in stacking together different images and reduce the stacked one. While the first gives its best for bright stars for which there is a high signal to noise ratio (SNR), the other is used to increase the SNR therefore is perfect for faint stars. It could seem that the second method is generally better
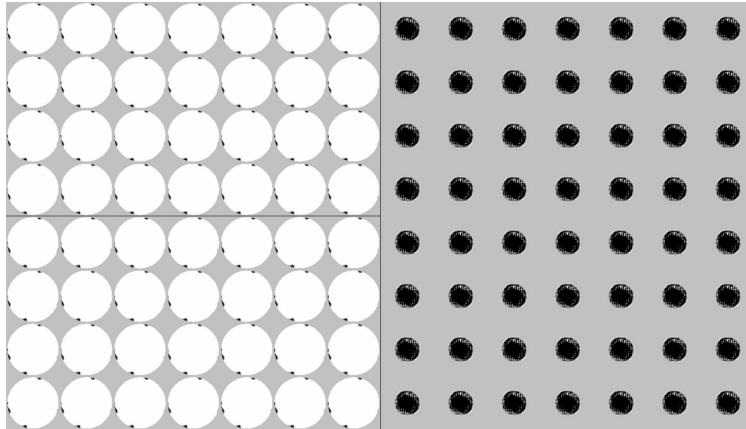
Figure 8: This is an example of PSF obtained for the image *icau23j6q* which is one of those taken in the filter F438W during E1. The grid is just a way the authors of the code used to represent the PSF.

than the first one but this is not true: in fact, stacking together images while improving the SNR for faint stars, strongly reduces the accuracy in the position of the stars, especially for the bright ones (compared to the other reduction method). Moreover, stacking together different images is an operation on the data and as such it brings along intrinsic uncertainties and systematics. These in principle are less relevant than the benefit the operation produce for faint stars but may be not negligible for bright stars which already have an high SNR. Since in this work I am mostly interested in RGB stars and upper MS stars that are quite bright, I decided to rely on the independent reduction of each image.

Therefore, for each image I run the code provided by J. Anderson and collaborators to get the best PSF in each frame starting from a reference PSF model, provided by the same authors, in each filter. I repeated iteratively this process three times using as model for each new iteration the PSF obtained at the previous run. An example of PSF obtained after this iterative cycle is the one reported in figure 8.

Once I have the best PSF for each image, I can use it to fit all the light sources in the image and separate good star candidates from noisy sources. To this aim, J. Anderson and collaborators provide another FORTRAN code called *img2xym* which takes as input the PSF obtained with the previous code, and HMIN, FMIN, PMAX defined exactly as before. Since now the aim is to detect as many stars as possible, the three parameters will be set to values completely different with respect to those used in the previous code where the aim was computing the PSF just around good stars. Therefore I decided to set HMIN, which is the minimum distance in pixels that nearby sources must have, to 3 pixels; the minimum flux (FMIN) to 50 counts in order to detect also very faint sources (which however for the majority will be noisy); the maximum flux (PMAX) to 99999999.9 counts in order to include also saturated stars. This latter value is arbitrarily set so high just to

be sure not to exclude possible saturated pixels.

The output of this code is a file .xym containing all the coordinates (x and y in pixel units), the instrumental magnitudes, and the values of the quality fit (*Qfit*) for each light source detected by the code. Moreover, in the same output file, are reported some other recap parameters. However, not all the sources identified by the code are real stars: a large fraction of them are noisy sources. Therefore, in order to reject as much noise as possible, I created a simple code aiming to keep just those sources considered stars and rejecting the noisy ones. It initially removes all those sources which are above a reference line constructed as quadratic interpolation of points selected by eye (see figure 9). The aim of this first cleaning is removing evident outliers. Then I divided the remaining sample in bins of 0.2 magnitude and for each bin I computed the median of *Qfit*. Finally, I rejected all those candidate stars of the sample which are more than two standard deviations above the median. This choice was arbitrary: it is an ulterior refinement of the cleaning. In the end I had a sample that is not affected by noisy sources. During this cleaning procedure I surely rejected also some possible stars but since the aim of this work is mostly concentrated on astrometry which, as discussed later, can be achieved with good accuracy just for bright and well detected stars, losing few sources won't be a major issue.

This procedure was repeated for all the images.

2.4   Photometric Catalog

Since the procedure described above creates a star catalog per each image, to merge them having an average instrumental magnitude for each star in each filter, I have to move each catalog into a unique reference frame. With this purpose Anderson and collaborators provide a code called *xym2mat* which computes the matrices for the transformation of the coordinates of an image, to those of a reference master frame. The procedure is based on finding similar triangles in the two images and then rotating and translating them until they coincide, obtaining this way the transformation matrices.

This code takes as input a file containing the name of the master frame (the image used as reference), and those of all the images that you want to combine; a code that indicates which HST's camera took the image and in which filter, and a range of magnitudes from which taken the good stars that will be used to compute the transformations.

Transformations from each star will bring to slightly different values for the coefficients, in particular, the fainter the star, the larger the residuals between the position in the master frame and the position in the rotated and shifted frame. Therefore, in order to maximize the accuracy (thus including the largest number of good stars over which computing the transformations) without affecting too much the coefficients, I decided to try different values for the magnitude range: while the brightest value was fixed to $-13.7mag$ which is the reference value above which stars include saturated pixels; for what concern the fainter limit, I started from a very faint magnitude (-6mag) moving it repeatedly toward brighter values until 95% of the residuals lay within 0.09pix. This way I was sure to include the
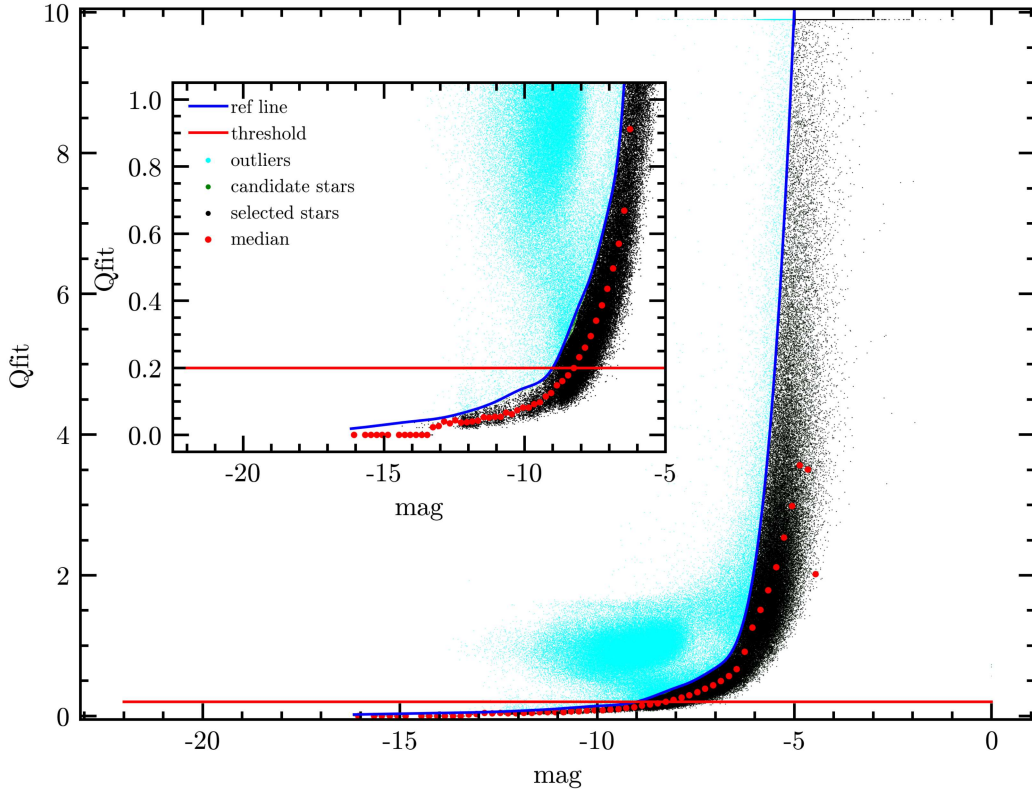
Figure 9: *Qfit* versus instrumental magnitude plot. This plot was drawn for each image. Here I report just one of them (Filter F275W, image icau23jaq, epoch E1) as representative example. Each dot represents a candidate star identified by the code. The blue line is the quadratic interpolation of points selected by eye to remove evident outliers (cyan dots). Red dots are the medians of the *Qfit* of candidate stars (green dots) in bins of 0.2mag. Black dots are the selected good stars. The red line corresponds to the value of QMAX used to select good stars from which sample the references used to compute the PSF.

maximum number of stars that grant me the accuracy of 0.09pix that I wished.

Once obtained the transformations from each frame to the master, the authors provided a second code called *xym2bar* which, starting from the transformations, identifies in how many frames a star is detected reporting as output the average magnitude and position. Since this code allows me to average out the stars' position and magnitude, in the input file I have to change the magnitude intervals such that all the stars will be included in the analysis and not just the brightest as done before. The magnitude range selected is then (-99.9, -5.0). Even if the code has detected some stars also fainter than -5.0mag, these are not well fitted by the PSF thus their error would be too large to be successfully used in the rest

of the work, therefore is better to reject them all at this level. However, as discussed later in this work, also stars fainter than -10.0mag are not enough accurate for an astrometric discussion but they are still important in the creation of a complete photometric catalog thus I decided to keep them.

At this point is interesting to notice that some sources detected in a certain image may are not in another. I refer to this kind of object as temporary sources, and the causes for these blinking (or rise in magnitude or even a complete vanishing of the source) can have different causes. In the majority of cases they are just noisy sources (mostly cosmic rays) which by chance where considered as candidate stars by the PSF fitting and therefore have to be rejected, but, on the other side, they may be variable stars which I will not reject. A powerful feature of the code *xym2bar* is the parameter NIMMIN which allows to set a minimum number of images in which the candidate star should be detected in order to be considered effectively as a star. This allows the rejection of cosmic rays and other noisy sources causing the presence of a temporary fake star, but it will also possibly reject real stars which, because of many different reasons, are not detected in all the images. For what concern the WFC3 camera where, in each filter, I have six images with almost the same exposure, I set this parameter to two such that if the source was detected in at least two images, then I can consider it as a real star. Referring to the ACS camera, I am forced to set this parameter to one. This because for each filter I have just two short exposure images used for the brightest stars in which the faintest are not detected and, as a consequence, in order to not reject all those bright stars that were detected just in one of the two, I had to set the parameter to one loosing the possibility to further remove possible temporary noisy sources. However, this will not be a major issue since the majority of noisy sources were already removed before through the $Qfit$ parameter analysis.

As said before, in addition to remove temporary noisy sources, this procedure allows also to detect variable stars which manifest themselves as sources in the same position but with a different brightness in multiple images. What I can do to detect them is looking for those sources which RMS on the magnitude is larger than the average of the RMS of stars in the same magnitude interval. This effect is evident just for bright stars where the RMS are sufficiently small to clearly disentangle noisy fluctuations in the brightness from a clear physical variation. An example is that reported in figure 10 where I plotted the magnitude variations as function of the magnitude itself in the filter F275W. It is clearly visible the presence of few tens of sources with a strong variability in the magnitude range [-12, -11]. A deeper analysis, matching the candidate variable stars in all filters, shows that almost all the sources identified in two or more filters lay on the horizontal branch, within the instability strip. Even if no further verification was carried out, I suggest that all these sources are RR-Lyrae stars. These are not particularly relevant for this work, thus are not further studied but, once identified, they can be flagged when saved in the final photometric catalog in order to use them in future works.

At the end of this process, for each filter, I will have a catalog of stars with the best achievable accuracy in position and instrumental magnitude. However, I still can not build
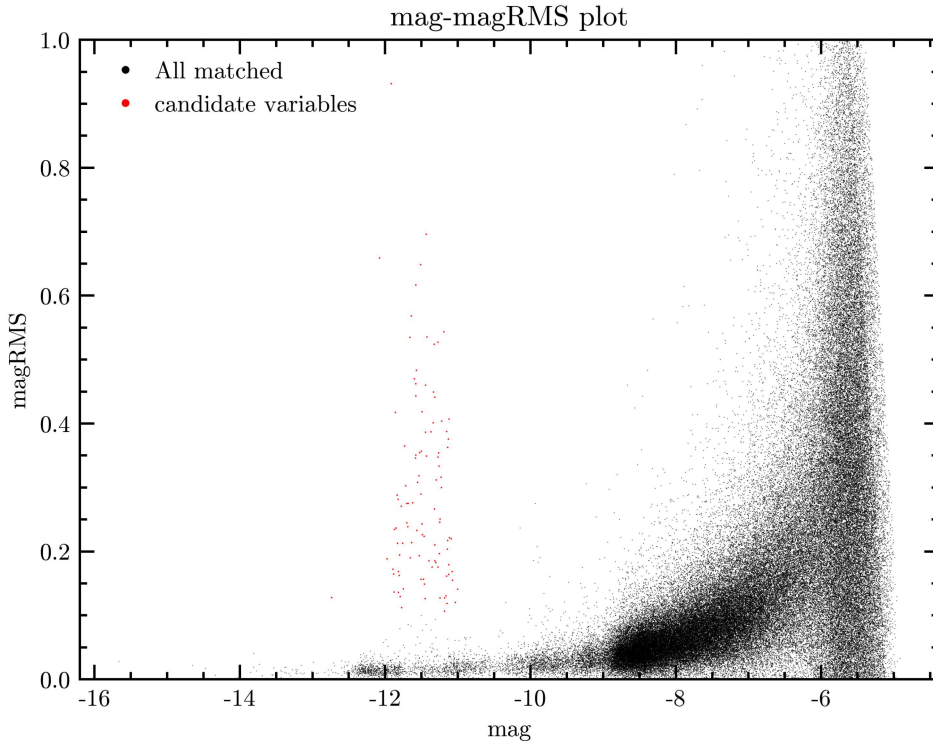
Figure 10: Plot of the magnitude variations of a source vs the magnitude itself. Red dots represents candidate variable stars. Plots like this have been built for any filter, here I reported as example just that relative to the filter F275W in E1.

the CMD since each filter is studied in the reference frame of its own master frame which is an image of that filter. Anderson and collaborators then provided another code named *xym1mat* which compares two catalogs in different filters and matches stars in common.

Since the filter F814W is the deepest one, with the largest number of stars detected, I used it as reference and through this new code I matched it with all the other catalogs obtaining a final catalog containing all the stars detected both in F814W and in any other filter.

In principle this would be the final photometric catalog, but it still refers to something somehow arbitrary: the coordinates of the stars are, in fact, all referred to the master frame of F814W.

In order to better generalize the catalog to a universal reference, I had to change the master with that of the Gaia satellite which is not relative as that of HST. Moreover, once moved to the Gaia's reference frame, the x-axis of the image will correspond to the Right Ascension (RA) while the y-axis to the Declination (DEC). In the following I will

still continue to refer to the axis as x and y with the meaning of RA and DEC. I made this choice to not confuse the reader with the coordinates since, while RA and DEC are normally referred to in angular units with the center of the reference system in the Earth, I will work with relative coordinates with the center arbitrarily set by the user.

To this purpose i downloaded from the Gaia's Archive[4] (van Leeuwen et al., 2021, González-Núñez et al., 2021) the Gaia's data centered in M 54 and within the firsts two arc-minutes. I had now to convert the coordinates of the sources in the Gaia catalogue from RA and DEC to the equivalent in pixels in order to have the same unit used by HST and therefore compare the catalogs. This process is done by a code provided by A. Milone and written in Supermongo language which automatically computes the transformation matrices that convert the angular units in the celestial sphere to linear units. The output will be the same of the original Gaia's one but with the coordinates converted from RA and DEC in degrees to pixels using as scale factor $0.04\,arcsec/pixel$ that is the HST resolution.

In order to use this new file as master frame, I need also to replace Gaia's magnitudes with HST instrumental magnitudes. With this aim I run the code *xym1mat* to match this Gaia's catalog with that of the filter F814W of HST. From the output file I can extract the coordinate in pixels units but in the Gaia's reference frame (thus with the axis oriented toward the common directions RA and DEC) and the HST's instrumental magnitudes. This can be used as new master frame for all the filters in order to bring all of them into the same reference system. Then I repeated all the procedure described before but this time in an iterative way. I run *xym2mat* and *xym2bar* to get new transformations in this new reference system creating this way a new catalogue for the F814W filter. Since this new catalogue was obtained using as reference just the few thousand stars identified by Gaia (which are much less than the three hundred thousand identified with HST in the filter F814W), I can strongly improve the quality of my analysis using the output of this first iteration which contains almost all the stars identified by HST as new reference for a second iteration. This way when I run for the second time *xym2mat*, the transformations are computed on a much larger sample of good stars, being therefore more reliable.

The master frame obtained after this second iteration for the filter F814W can be used also for all the other filters without the need of the double iteration. This way all the filters will be transported in the reference frame of the filter F814W (which thanks to the last passages coincide with that of Gaia) and can be easily compared together simply running the code *xym1mat*. Doing this I match all the filters, one by one, with my reference: F814W. I choose it as reference because it has the largest number of detection.

This procedure creates the photometric catalog containing all the photometric information of stars detected in the HST's filters F275W, F336W, F438W, F606W and F814W with the positions of the stars expressed in pixels and in the Gaia's reference frame. Using the data stored in the catalog I am able to build the CMDs shown in figure 11.

Since I have not brought the magnitudes in a reference system like that of Vega, the

---

[4]https://gea.esac.esa.int/archive/

magnitudes are still instrumental. Being HST a space-telescope, the conversion of the instrumental magnitudes into the common systems is obtained simply adding a constant retrieved comparing this catalog to a reference one already in the Vega's reference. However, since working in the instrumental or in the Vega's system there are no substantial differences for the kind of work carried out hereafter, I decided to remain in the instrumental one.

Thereafter I will refer to the instrumental magnitudes simply as magnitudes.

(a) F275W-F814W

(b) F336W-F814W

(c) F438W-F814W

(d) F606W-F814W
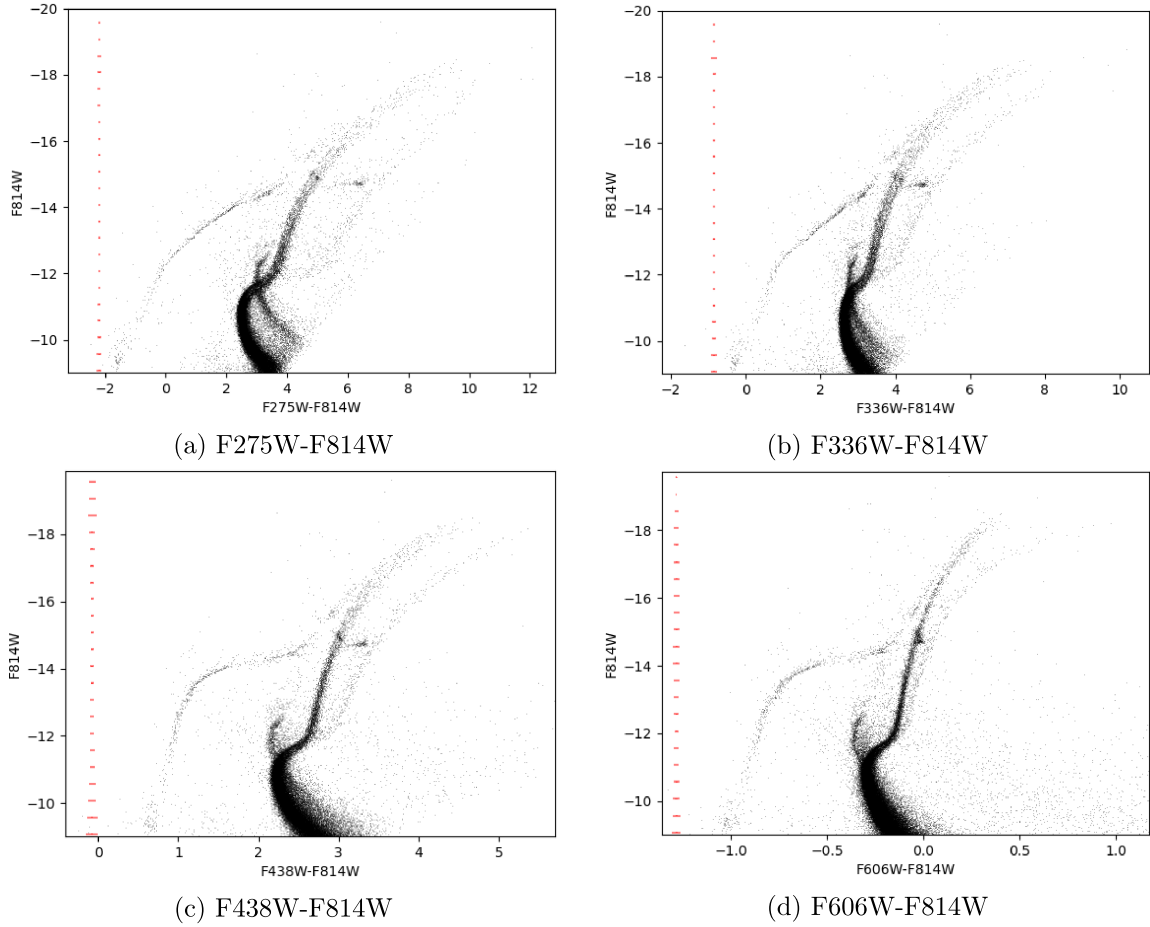
Figure 11: These images are the CMDs drawn using data from the photometric catalog just built. All these CMDs are built combining one HST filter with the reference F814W, against the magnitude F814W. On the left of each CMD are reported in red the median uncertainties of stars in bins of 0.5mag. No differential reddening correction is applied. Comparing figures 11a and 11d is evident how a wide color baseline separate the young populations from the older ones more clearly than a narrower one. See also that the optical filters F606W and F814W are those with the highest accuracy, indeed the uncertainty on the color is the lowest in the the CMD 11d. Observe also that in the UV CMDs bright stars have a color uncertainties that grows with brightness: this is because some pixels in the PSF of these stars were saturated thus the real flux is inferred from the PSF's shape, with a corresponding increase in uncertainties.

2.5   Proper Motions determination

As previously discussed in section 2.2 and listed in Table 1, HST images are collected in three different epochs along a period of 8 years.

Working with images taken among different epochs allows to compare the star's position on the celestial sphere at different times thus recovering its proper motion.

The photometric catalog previously realized cannot be used to infer proper motions since to create it I have studied together images with the same filters but collected in different epochs, averaging out the information on proper motions in favour of an higher photometric accuracy. Therefore all the procedure done previously have to be repeated analyzing each filter in each epoch separately.

Since the PSF analysis and the extraction of good candidate stars was already done for the photometric catalog analysing image by image separately, I can start from here my new analysis.

Having for each epoch in each filter at least two images, I need firstly to bring them in a common reference frame in order to average them out. Aiming this I used the code previously discussed *xym2mat*. As master frame I selected the same master frame used for the photometric catalog in the Gaia's reference frame. This way I have the highest statistic (because this catalog contains all the stars detected in the filter F814W) and all the images will be brought in the same reference system. For the selection of the magnitude range from which extract good sources for the determination of the coefficients for the transformations, I adopt the same procedure illustrated before: I fixed the brightest magnitude to -13.7mag (limit for saturation) and the faintest to -6mag, then I iteratively run the code moving the faintest magnitude toward brighter values (doing steps of 0.1mag) up to when 95% of the residuals lay within 0.09pix. Subsequently I used the code *xym2bar* to compare the images in the same epoch and same filter and detect stars in common. As largely discussed for the case of filters F606W and F814W in section 2.4, I am forced to set for each filter and each epoch a value for the parameter NMIN equal to one. This because for all the UV filters there are just three images per epoch thus, asking for sources detected in more than one image would possibly cause the loss of few good sources detected by chance just in one of the three images.

This procedure is repeated a second time using as new master the catalog obtained as output of the code *xym2bar*. This passage is necessary to have a master which sources are effectively those detected in that frame, ruling this way out a possible loss of proper motion information related to a too general master frame. Using these codes I have for each star, in each filter, at each epoch, the magnitude and the position both with the respective root mean square error (RMS).

This procedure is done just for the WFC3 filters because are those taken in two different epochs. For what concerns the two filters of the ACS camera, since images are taken just during E0, the data reduction already performed to build up the photometric catalog is enough.

Finally, using the code *xym1mat* previously discussed I matched the catalogs obtained per epoch and filter with my reference that is the catalog of the filter F814W obtained at epoch E0.

J. Anderson and collaborators provide also a code called *lnk2res* which is similar to *xym2mat* but while this latter provides the coefficients for global transformations to align the frame with the master, *lnk2res* compute the parameters for local transformations in order to have the most accurate displacements with respect to some reference stars user provided. In detail, the inputs required by the code are:

lnkfile Is the catalog (output of *xym1mat*) containing the stars for which we want to compute the accurate displacement on the celestial sphere.

NITu Is the number of iteration that the code will perform in order to obtain the most accurate values. At each iteration the code will discard some good stars since according to its analysis they are not sufficiently good references. This way at each iteration the code automatically refine the set of reference stars to use in order to infer the most accurate displacements. Since I start from a well defined sample of stars as reference, two iteration are sufficient.

RADU Is the radius of the circle within which the code takes the reference stars necessary to compute the transformations.

UFILE Is the path of a file containing a flag that is set to one if the star is considered as a good reference, to zero otherwise.

To properly fix the zero point, the authors suggest to select a sample of reference stars which should share similar kinematics.

Making advantage of the photometric catalog previously created as described in section 2.4, I broadly isolated by eye the stars in the old population and in the younger excluding blue stragglers, horizontal branch stars and, as far as possible, binaries. This first isolation of the populations is very broad and rely on a cleaning made removing by hand stars which membership of the populations was doubt. For this cleaning I looked just at the CMDs made with the color F275W-F814W and the pseudo-color F275W-F336W-F814W against the magnitude F814W. I did not performed a more refined cleaning relying also on other CMDs in this part of the work simply because the ulterior refinement of the samples is made by the code *lnk2res* itself. A more refined separation of the young and old populations is necessary for the second part of the work and is described in section 3.1.

Once created the flags catalog, I run *lnk2res* setting NITu to two and trying different values for the parameter RADU. I made a first try considering as good references just the stars of the older population and a second one considering as reference both the stars of the old and the young populations. To determine which sample of reference stars and parameters combination performs better, I plotted the displacement dr of each star vs the magnitude. The value of dr is obtained as $dr = \sqrt{dx^2 + dy^2}$ where dx and dy are the

output of the code managed with the same procedure adopted for the $Qfit$ analysis in section 2.3: I initially draw a curve used to remove the evident outliers selecting by eye some reference points and interpolating them; then, on the remaining values, I computed the median in windows of 0.25mag and interpolated it with the magnitude of each star obtaining a smoothed curve with the values of dx and another one with the values of dy for each magnitude.

The combination of reference stars and parameters that gives the lowest displacement is the most reliable one since is that with the better defined zero-point. The larger the reference sample the better it is, therefore consider as reference both the young and the old populations is in principle the best thing to do. However, aiming this, I had to check that including or not the young population in the references would not highlight a bimodal distribution in the plot $\mu_\alpha cos(\delta)$ vs μ_δ which implies a different mean motion of the old and young populations.

Once verified that including in the reference sample the young populations there is not the formation of the bimodal structure, I am allowed to consider the reference sample as the one made by both the young and old stars.

The fact that there is no bimodal distribution (i.e. that the shape of the proper motion distribution does not change) is the first result of this work: from the physical point of view this means that the average motion of the old population and of the young is the same. This outcome was not a foregone conclusion since a priori there are no reasons to assume that the two populations share the same mean motion.

Fixed the reference sample, I tried different combinations of parameters (see figure 12). Although I noticed that there is no big difference in choosing one combination of parameters or another, it seems that setting the value of RADU to 300pix and iterating two times (i.e. using as UFILE for the second iteration a file containing the reference stars refined by the first run of the code), gives on average a value of dr slightly smaller, especially for the fainter magnitudes.

At the end of this process I have, for each star in each filter at each epoch, the displacement dx and dy relative to the reference epoch E0; the coordinates of the star detected in the filter F814W that is my master; two values named Sx and Sy for the RMS of the star's position in the x and y axis. These are sufficient to get the proper motions combining the stars' position at different epochs.

This procedure won't give absolute displacements but relative to the sample of reference stars within the radius RADU.

The accuracy on relative quantities is definitively higher than that on the absolute ones, but relative quantities kill some information which may be fundamental, for example the rotational curve.

Gaia satellite measures proper motion in an absolute way but it is not able to infer them for lot of stars up to the distance of $M54 + Sgr$ (26.5kpc according to Harris, 1996, 2010 edition). In principle, there are few ways to relate Gaia and HST data in order to obtain absolute proper motions for all the stars detected by HST but this is not the main target
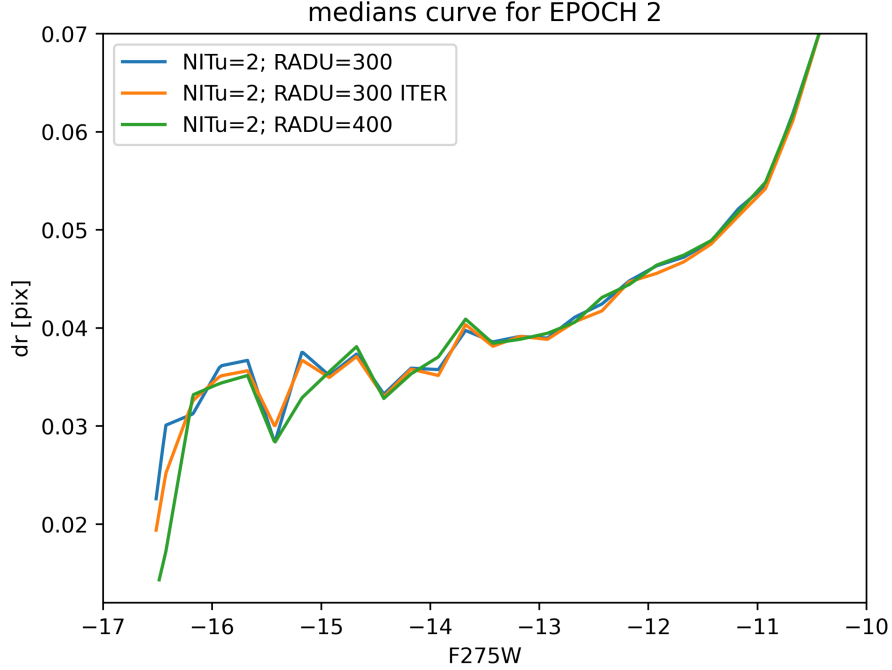
Figure 12: Plot of *dr* versus the magnitude in the filter F275W. The blue and the green lines are obtained setting as reference stars both the old and the young populations and the two differs just by the value of the parameter RADU which is 300pix for the blue curve and 400 for the green one. The orange line instead is obtained running iteratively the code *lnk2res* a first time using as reference stars the same adopted for the other two lines, while for the second run it uses as reference stars those selected by the code at the first iteration.

of this thesis thus won't be further explained (if interested in the procedure, see Cordoni et al., 2020a and references therein).

Knowing the relative displacement obtained as output of the code *lnk2res* I have to set the time in coordinates usable to recover the proper motions. I created a python code which firstly converts the epoch from the UTC format *yyyy/mm/dd hh : mm : ss* into the more manageable JD format relying on the python *astropy* package[5] which is provided with a function that automatically makes the conversion. Although in principle can be chosen as representative time for each epoch the time of the first image taken at that epoch, I decided to use as representative time for my study the median of the times at which all the images

in that filter, at that epoch, were taken. This is an arbitrary choice since images per filter and per epoch are taken within hours or at most few days (see Table 1) thus the motion on the celestial sphere in this short period is completely negligible. I normalized all the JD epochs by 365.25 in order to change units from days to years making the values more readable.

I choose as starting reference time the median JD time of the F814W observations and I shifted all the other epochs with respect to this value in order to have my reference starting point in zero. This way, since images in the filter F606W were taken few hours in advance with respect to those in filter F814W, the shift will brings the time for F606W to a negative value which seems unphysical but it is just matter of reference point, thus just a mathematical artifact with no real meaning.

The code takes as input all the catalogs created per filter and per epoch and transforms the quantities dx, dy, Sx, Sy from pixels to milli-arcseconds multiplying them by the scale factor used also previously $40\,mas/pix$.

I replaced for each star the associated RMS-errors Sx and Sy with the median of the same quantities of all the stars with the same magnitude. This median curve was computed with the same procedure explained multiple times above: firstly I removed the evident outliers drawing a curve by eye, then I computed the median of the remaining stars in windows of width 0.51mag and finally I interpolated these values for all the magnitudes of the stars in my data-set (from now on I will refer to this new estimator of the uncertainties on the position of the stars as ERR_x and ERR_y). The evident outliers discarded with this cleaning are sources for which I will not compute the proper motion.

Conceptually this procedure assumes that all the stars with the same magnitude should be characterized by the same uncertainty on their position, this is why, as estimator of the error, I am allowed to use the median of the RMS of stars sharing the same magnitudes. Since the position is obtained averaging the position of the star in each image in which it was detected in that filter at that epoch, I also expect that the uncertainty associated to stars detected in more than one image is lower than that of stars detected in a single image. To add this feature to the quantities ERR_x and ERR_y of the stars in my data-set, I normalize these two quantities by $\sqrt{N_{det}}$, where N_{det} is the number of images in which that star was detected for a fixed epoch and filter. This last equation is true if the number of samples N_{det} tends to infinity, but this is not the case. According to Stetson (2005) the distribution of the RMS computed from a limited number of samples is more similar to a Student's t-distribution than to a Gaussian and therefore has to be multiplied by a corrective factor to get the corresponding standard deviation. According to him this factor is $\frac{N_{det}-1}{N_{det}-1.5}$. Obviously in the case in which there is just one detection this factor become zero, but this is irrelevant for what concern the study of proper motions since we need a minimum of two detection in two different epochs.

The procedure described above is used to create a catalog for each filter and epoch containing dx and dy, ERR_x and ERR_y (corrected) for each star detected.

To infer the proper motion of a star the procedure adopted is the following:

1. Select a star from the photometric catalog which include all the detected stars.

2. Search for this star in each catalog just created per epoch and filter and from each one import dx and dy, ERR_x, ERR_y and the JD time relative to that catalog and shifted according to the chosen reference point. This will create a new data frame in which each row corresponds to the star's displacement, with relative uncertainties, in a different filter and epoch. Having two filters in E0 and three filters in E1 and E2, the maximum number of detection for each star will be 8.

3. Perform a linear fit of the quantity dx as function of the time coordinate in JD years weighting each point with the relative uncertainty ERR_x. Repeat for dy.

4. Repeat for each star in the photometric catalog.

The python code that I wrote to infer the proper motions performs the linear fit through the function *Curve Fit*[6] of the *scipy*[7] package which as outputs reports both the intercept and the slope of the straight line that best fits the data. I am not interested in the intercept since it represents the position of the star at the reference epoch (i.e. the star position at the time in which the images of the filter F814W were taken) assuming true the linear relation with the temporal coordinate, since I already have the true position in that epoch. The slope instead corresponds to the proper motion of the star in the direction x (or y) in the Gaia's reference frame, therefore RA (or DEC), in units of mas/yr.

An example of the fit is that reported in figure 13.

It may be that some stars in the photometric catalog were detected just in one epoch. For these stars it is impossible to compute the proper motion since for the linear fit at least two points are required. Instead, mathematically speaking, it is possible to infer the proper motion of a star detected in two filters during the same epoch but the result will be unphysical: since observations within the same epoch are taken with a temporal baseline of few hours (few days at most), the star's motion is undetectable on a so short baseline (any apparent displacement is just caused by errors), therefore the result of the fit will be meaningless.

In order to speed up the procedure I did not compute the proper motions for those stars which are detected just in E1 and E2 (year 2013 and 2014) because the temporal baseline of just one year is too short to grant a sufficiently accurate proper motion.

Images in different epochs and filters are slightly shifted or rotated with respect to each other (see figure 14). As a consequence, it is not unusual that stars in the outskirts of the field are detected in just two filters therefore proper motions inferred for the outer regions are less accurate than those for the mid regions of the field (uncertainties on ERR_x and ERR_y are larger because of the lower number of detection, and having just two epochs also the uncertainties on the fit's parameters are larger). Also in the central part of the field

---
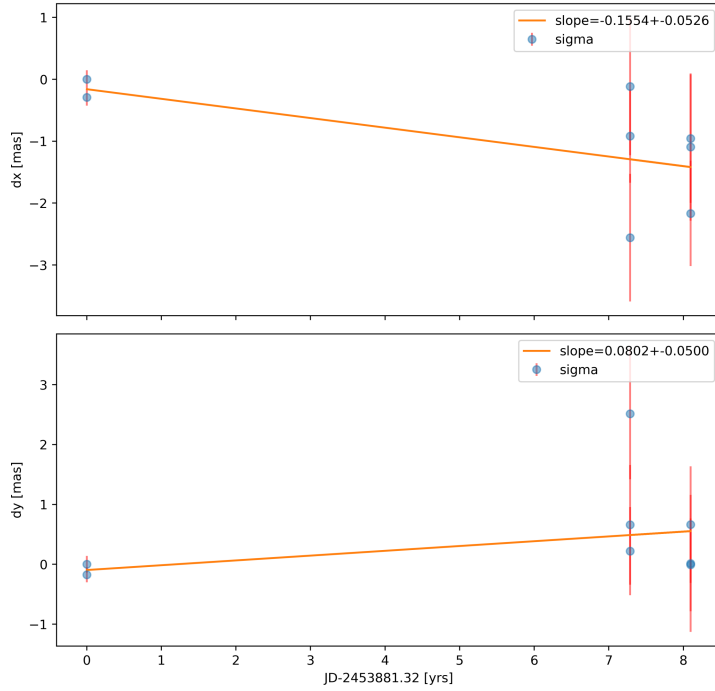
Figure 13: Representative example of the fit done for each single star to infer the proper motions along the two directions.

proper motions are measured just for few stars: this because M 54 is a very dense cluster and the central region is too crowded to clearly disentangle and follow sources with the required accuracy using the codes provided by J.Anderson and collaborators.

The whole procedure described here above allowed me to build the astrometric catalog containing the proper motion along RA ($\mu_\alpha cos(\delta)$) and DEC (μ_δ) of stars in the field.

Thereafter in this work I will refer to the number of detection in each filter and epoch simply as *epochs*. Therefore, saying "the star was detected in 8 *epochs*" I mean that it was detected in all the filters in E0, E1 and E2.

2.6 Radial and tangential components of proper motions

Proper motions determined up to now are referred to the x and y axis of the Gaia's reference system relative to an ensemble of nearby stars. Interesting properties of the system can be inferred looking at the same quantities but in polar coordinates centered in the cluster's center. Once done this change of reference system I will have the proper motion in the radial (apparent motion toward the center of the cluster) and tangential direction.

Aiming this, I first need to find the center of the cluster: in first approximation I can choose the center of the cluster simply as the center of the distribution of all the stars
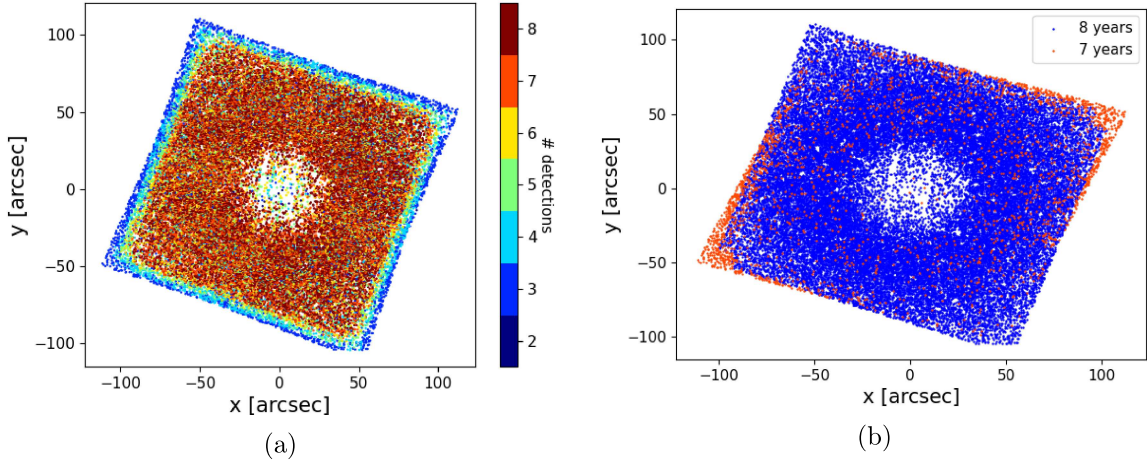
Figure 14: On the left is reported the distribution of stars coloured by the number of epochs and filter in which they were detected. On the right stars are colored by the temporal baseline used to infer the proper motion.

detected in F814W (the filter with the larger number of detection), this method however would give a reliable set of center's coordinates just if the stars detected are characterized by circular symmetry. A more powerful method is that suggested in the paper Cordoni et al. (2020a). The procedure developed by the authors consists in fitting concentric ellipses on the star spatial distribution and then take as center of the cluster the median of the centers of all the ellipses. This method allows also for a non circular symmetry of the sample of stars being therefore more reliable than the previous.

Instead of using as set of stars from which get the center of the cluster all the stars at my disposal, which includes also background and foreground objects, I rely on the populations already flagged in order to use the code *lnk2res* as explained previously in section 2.5. Plotting the contours of the old and young populations I saw that this latter is characterized by an elongated elliptical shape, while the old population shows a circular symmetry. The morphology of the populations will be further studied in section 4.1. Being the old population characterized by circular symmetry, the determination of the center would be affected by less systematical. Therefore, I selected stars of this population to find the center of the system.

Having the center of the cluster with its own error estimated as the standard deviation of all the centers of the ellipses, I can convert the proper motions in polar coordinates. Firstly I shift all the system with respect to the center just computed such that the center would have coordinates (0,0). Then I split the field in quadrants and define for each quadrant the angle θ as the angle between the vector joining the center of the field with the analyzed star and the x axis: mathematically speaking $\theta = \arccos\left(\frac{x}{\sqrt{x^2+y^2}}\right)$. According to this

definition for each star in each quadrant the transformation for the proper motion in the x and y axis into radial and tangential are given by a rotation of the angle theta which can be achieved using trigonometrical functions.
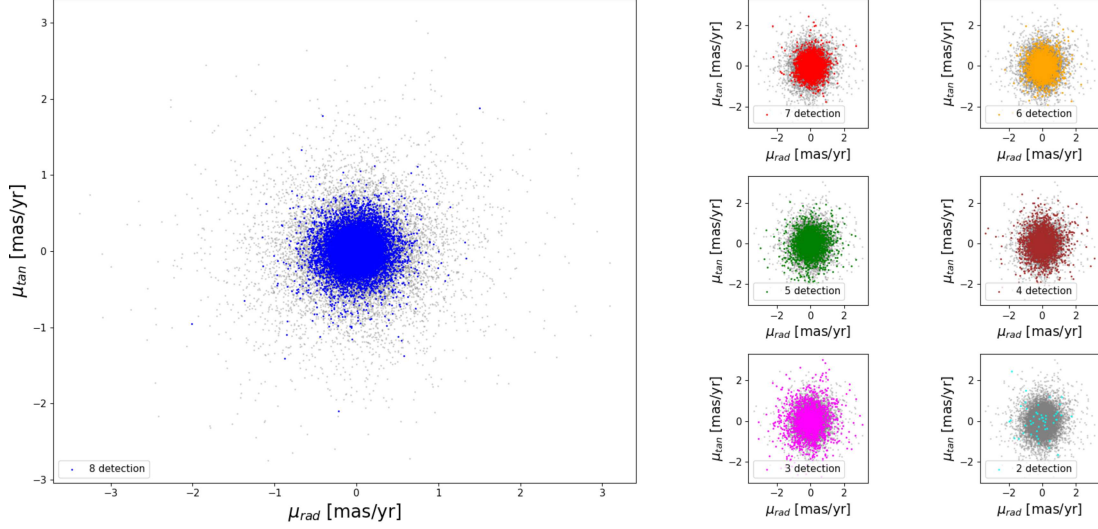
Figure 15: This panel shows the distribution of the proper motions along the two axis (radial and tangential), one relative to the other. In the larger plot are shown stars detected in all the 8 *epochs* while on the right are shown stars with less than 8 detection, from 7 in the upper left to 2 in the lower right. As reference, colored in gray in the background, are shown all the stars for which there is the measure of proper motion. This plot considers stars with magnitude between -17 to -9 F814W.

The errors on the proper motions expressed in these new coordinates are computed as propagation of the errors over all the operations done. Therefore, the shift with respect to the center of the cluster will results in an uncertainty on the stellar position given by $\sigma_x = \sqrt{ERR_x^2 + \sigma_{xc}^2}$ (same for the y axis), where ERR_x is the original uncertainty on the star's position obtained previously during the creation of the astrometric catalog, while σ_{xc} is the uncertainty on the location of the center of the field and obtained as standard deviation of the center of the ellipses used to find the center itself. The error on the determination of the angle θ is given by $\sigma_\theta = \sqrt{ERR_x^2 \left(\frac{y}{(x^2+y^2)^2} \right) + ERR_y^2 \left(\frac{x}{(x^2+y^2)^2} \right)}$. With this procedure I obtained the radial and tangential projections of the x and y components of the proper motion of each star. To finally have the radial and tangential components I summed the projections of the x and y axis along the same direction. Finally the uncertainty on the tangential and radial components is computed as quadrature sum of the uncertainties of

the projections which are given by:

$$
\begin{cases}
\sigma(P_{x-rad}) = \sqrt{\sigma_{xc}^2 \cos^2 \theta + \sigma_\theta^2 P_x^2 \sin^2 \theta} \\
\sigma(P_{y-rad}) = \sqrt{\sigma_{yc}^2 \sin^2 \theta + \sigma_\theta^2 P_y^2 \cos^2 \theta} \\
\sigma(P_{x-tan}) = \sqrt{\sigma_{xc}^2 \sin^2 \theta + \sigma_\theta^2 P_x^2 \cos^2 \theta} \\
\sigma(P_{y-tan}) = \sqrt{\sigma_{yc}^2 \cos^2 \theta + \sigma_\theta^2 P_y^2 \sin^2 \theta}
\end{cases}
$$

At the end of this procedure I have the proper motions in polar coordinates relative to the center of the cluster (see figure 15).

3 Data Analysis

In the previous section of this work I explained how I managed the raw multi-band and multi-epoch HST's images in order to create a photometric and an astrometric catalog. In this section I will explain how I used the photometric catalog to broadly isolate the populations in the system and the astrometric one to analyze their kinematical properties.

3.1 Identification of the populations

Combinations of CMDs represents one of the best ways to divide stars in populations sharing the same properties. The paper Siegel et al. (2007) is one of the most accurate in terms of identification of populations in the system $M\,54 + Sgr$, identifying up to four different populations with different ages. However, in this paper was not possible to clearly disentangle stars in the MSs and SGBs of the different populations since in the color F606W-F814W these are overlapped thus, the authors infer the presence of the populations through isochrones fitting and simulations, relying mostly on RGB and few SGB stars. This was a limitation of their study related simply to the fact that in 2007 HST had not already taken the images of the system in the UVIS filters. These were firstly used in the paper by Milone (2016) which however was mostly focused on the identification of multiple populations within the GC $M\,54$ than on all the populations in the system $M\,54 + Sgr$.

In this work instead I am interested in knowing to which population stars belong in order to study their kinematical properties.

The peculiarity of multi-band HST images is the possibility of drawing multiple CMDs each one highlighting different features.

To divide stars in their own population from the CMD, it is firstly necessary to be sure that the stars' color and magnitude are not affected by systematics which mix stars in the CMD, like differential reddening.

Using the procedure described in Milone et al. (2012) which consists in deriving a fiducial line for the populations and then, for each star "A", taking the nearest N (on the plane of the sky), compute their distance from the fiducial and correct the color and magnitude of "A" by the median of this quantity. The procedure is done in an iterative way up to when the new differential reddening corrections become negligible. The choice of the factor N is very arbitrary since the larger N is, and the more reliable is the correction, but on the other hand, a larger N means also considering stars further and further apart form the reference "A" therefore loosing the locality of the correction.

Applying this procedure for the differential reddening correction trying different values for N (ranging from 20 to 50) I found that independently from the value of N used, no substantial improvement was obtained. I conclude that the system $M\,54 + Sgr$ in the circular region of 2 arc-min is not very affected by differential reddening.

The differential reddening correction is a procedure which directly acts on the magnitudes of the stars. It can be very powerful in the case of clusters strongly affected by

differential reddening where the correction is larger than the systematics introduced by the procedure itself, but if the correction obtained is very small, as in the case of the system $M\,54 + Sgr$, is better to avoid it in order to be sure not to add systematics to the data. Therefore I decide to reject the differential reddening correction just computed and for the next of this Thesis I will work on the original data.

Since this work aims to study the kinematical properties of the populations composing the system (which are reliable just when the population includes a large number of stars) I firstly split the stars in two macro-populations: the "old" one containing the stars considered in literature as part of the GC M 54 possibly mixed with an old component of the galaxy, and the "young" one containing stars part of the intermediate age, young and very young populations. I decided to split the system in these two for multiple reasons: firstly, in the literature authors always refer to the oldest population as that of the cluster, and all the younger as part of the galaxy but there is no clear reason for this identification therefore it might be interesting studying the kinematics of these two systems and see if they share similar properties or not. Another reason is related to simplicity: even using multi-band photometry is not easy to split the mid and lower MS of the intermediate population from that of the younger thus treat them as a unique population is a forced choice. Moreover, the youngest population does not have a lot of members therefore it may be that its kinematical properties will be dominated by stars' peculiar proper motions more than by global features. Considering instead all the populations younger than the old one as a unique population will strongly increase the number of stars over which average out the kinematical properties. Obviously, considering all these stars as member of the same population is a strong simplification which means averaging out possible physical differences among them.

For the splitting of the system in these two macro populations I rely on the combination of different CMDs, keeping in mind that I'm not interested in an exact splitting since for the study of kinematical properties I will refer to statistical quantities computed over all the stars of the same population. Thus, if few stars of the old population are flagged as stars of the young (or vice-versa), this will not be a major issue since these will be just few stars over all the population. Therefore, it is unnecessary to implement complex mechanisms of simulations to assign each star to a population but a splitting by eye is more than enough.

Firstly I noticed that the young population is quite well separated from the old population in the pseudo-color $(m_{F275W} - m_{F336W}) - (m_{F336W} - m_{F814W})$ thus I initially separate them simply with a line drawn by eye. However, in this color the bright stars of the young population are crossed by the horizontal branch's stars (HB) of the old population. I isolated old HB stars from the CMD in the pseudo-color $(m_{F275W} - m_{F336W}) - (m_{F336W} - m_{F438W})$ and then I removed it from the young population isolated in the previous CMD. From the pseudo-color $(m_{F275W} - m_{F438W}) - (m_{F438W} - m_{F336W})$ I also isolated the RGB of the old population, the RGB and the red clump of the young population and other main sequence stars that were not flagged in the previous filters. Once I have broadly isolated

the two populations by eye from these pseudo-colors, I refined them separately. For what concern the old population, I took the result of the cleaning from the pseudo-color and I built the CMD in the color $F606W - F814W$. I drown by hand two reference lines which encloses the old population and I rejected (i.e. I do not consider as member of the old population) all the stars that are out of these fiducials. The procedure is repeated on the colors $F438W - F814W$, $F336W - F814W$ and $F275W - F814W$. In the end I have a well defined MS, SGB and RGB for the old population. During this last cleaning I also removed horizontal branch's stars. This because the characterization of the photometry of very blue stars is not deeply studied and possibly their PSF fitting is biased (especially for what concern blue filters) by the intrinsic nature of these stars which, being hot and blue, tackle the performance of the instrumentation; therefore these stars would be probably characterized by spurious proper motions which would affect my analysis, thus, I decided to exclude them from the study. For what concern the young population, again I started from the cleaning made on the pseudo-colors and I improved it with the technique of the two fiducials in the color $F275W - F814W$ used also for the cluster.

This cleaning was done on the photometric catalog that is the one with the highest photometric accuracy, however, with the procedure described in section 2.5, I was not able to recover the proper motion for all the stars, therefore an ulterior cleaning consists in keeping just those stars for which I was able to get the proper motion. In addition, I made an ulterior refinement rejecting also all those stars which proper motion was definitively larger than that of stars with the same magnitude (in other words, I rejected evident outliers).

Using the cleaning procedure described above I have surely rejected a lot of stars which were member of the old or of the young populations and surely is possible that few stars of a population were flagged as member of the other, but as already mentioned this will not be a major issue. This procedure is fast compared with more refined techniques and, despite all, the quality of the splitting is sufficient for the kind of analysis that follows.

The result obtained at the end of the cleaning procedure is that shown in figure 16. In particular, after all these cleaning I have catalogued as "old" population 28364 stars with magnitude (filter F814W) in the range [-17, -9] and 3151 as "young" population in the same range. The brighter limit was set to -17mag F814W because I was not able to obtain the proper motion of stars brighter than this value because of the large errors associated to their position.

I also flagged the sub-populations of M 54 using the Chromosome Map. To build it I adopted the same procedure described in section 1.1: I took the RGB stars of the old population (which, as shown in figure 16, are those brighter than magnitude F814W - 12) and I built two fiducials, one relative to the 4th percentile of the spread in the color $F275W - F814W$ and in the pseudo color $(m_{F275W} - m_{F336W}) - (m_{F336W} - m_{F438W})$ and the other relative to the 96th. I rectified them according to equations 1 and 2, where the values for $W_{F275W,F814W}$ and $W_{F275W,F336W,F438W}$ were computed as the distance of
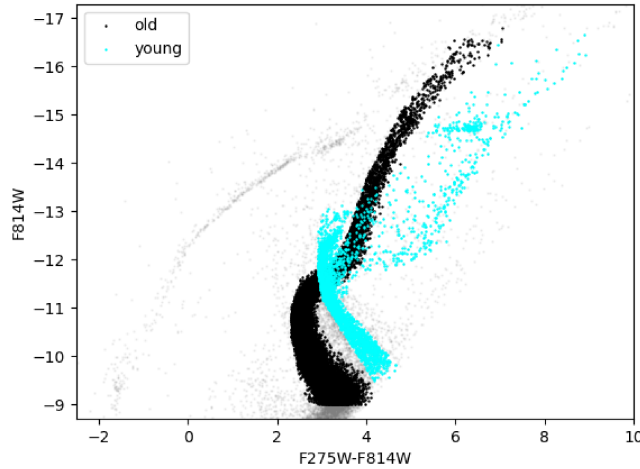
Figure 16: Here are shown the isolated old (black dots) and young (cyan dots) populations after the cleaning procedure described in the text. In background are visible all the stars detected in the photometric catalog from which stars of the two populations were isolated. Horizontal branch stars were removed as well as all those stars for which was not possible to infer the proper motion. The stars catalogued here as young population include those identified by Siegel et al. (2007) as intermediate, young and very young.

the two fiducials two magnitudes above the Turn Off point. This latter was obtained as the bluest point of a fiducial built as the median of the colors in magnitude bins of width 0.1mag in the filter F814W. The rectifying procedure produces two delta-quantities which plotted one against the other constitute the Chromosome Map. Then I roughly isolated the populations in the classical 1G and 2G, and the Anomalous simply drawing few lines by hand. Again, even if exist much more accurate procedures to identify the populations, and even if few stars of a population are catalogued as part of another, this will not be a major issue since kinematical properties are inferred over large samples thus the contamination of just few stars is negligible. The result of the splitting is showed in figure 17a. However, contamination among populations, even if not a dominant parameter in a kinematical study, may be relevant during the analysis of the spatial distribution of the stars belonging to different populations, especially when one compares the spatial distribution of populations identified with just few samples, as those detected from the Chromosome Map of the RGB of M 54.

The identification of the Anomalous population visible in figure 7 done by Milone et al. (2017) is more refined than that carried in this work.

While the Chromosome Map is a fundamental tool to identify sub populations from stars in the RGB with a small relative difference in the fraction of light elements, CMDs remain the best tool to identify multiple populations differing for large values of metallicity, age, rotation, distance and helium fraction. An important signature already discussed in

46

literature (see section 1) is that Anomalous GCs show a splitted SGB. M 54 is no less: from the CMD in the color $F275W - F814W$ (figure 11a) is clearly visible this splitting. Since the two populations defined by this splitting are worth to be investigated also from a kinematical point of view, I tried to separate them in two ways. Firstly I build up a Chromosome Map with the same procedure used for the RGB but this time on the SGB, between magnitudes F814W -11.3 and -11.9 and it appears as two clumps partially overlapped. I concluded that it would not be easy to separate them clearly from the Chromosome Map. Therefore I rely on the second way: drawing by eye a line on the CMD which would be taken as reference for the separation. I checked on the Chromosome Map of the SGB the result of the identification of the two population from the CMD and indeed the two clusters identified by eye were splitted quite well. The Chromosome Map of the SGB, with the two populations highlighted, is that shown in figure 17b. Since I will not assume any correlation a priori between the populations identified from the RGB and the SGB I will not refer to the two populations identified in the SGB as 1G and 2G but as Faint and Bright (since they describe respectively the faint and bright SGB of the old population).

(a) RGB Chromosome Map   (b) SGB Chromosome Map
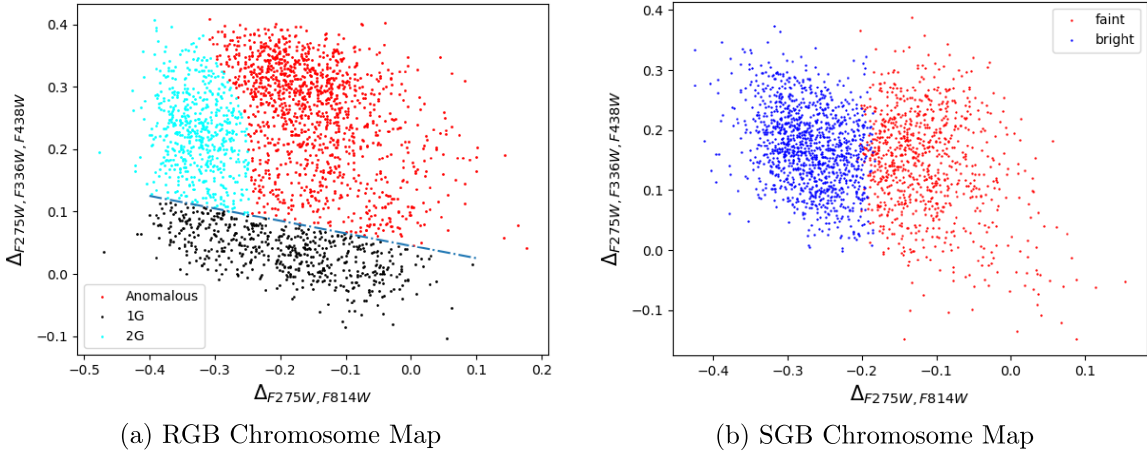
Figure 17: On the left is shown the Chromosome Map of the RGB of the old population. Black dots are the 1G, cyan dots the 2G and the red dots constitute the Anomalous population. Differences with respect to figure 7 are due to a slightly different choice of the zero point. On the right is shown the Chromosome map of the SGB with the identification of the populations done drawing a reference line on the CMD dividing the bright one from the faint one. Here the two populations are referred to simply as Faint (blue dots) and Bright (red dots) since I will not assume a priori any correlation with the populations found from the analysis of the RGB.

3.2   Tools for the analysis on the internal kinematics

The proper motions inferred as explained in section 2.5 are relative to the neighborhood of each star. This means that when in this work I refer to proper motion, in reality I am referring to relative quantities.

As shown previously in figure 15 the distribution of proper motions conceptually can be seen as a bi-dimensional Gaussian centered in zero. Therefore, to infer the kinematical properties of each population, I can not rely on the median of the distribution since for a sufficiently large sample this will be zero because of the method used to get the proper motions. A much more manageable quantity to use as estimator of the kinematical properties is the velocity dispersion. Mathematically this quantity represents the spread of the distribution of relative proper motions for the selected group of stars. There are many ways to estimate it, for example one can be through the standard deviation of the distribution, another can be through the 68.27^{th} percentile. In this work I used this latter which is less sensitive to the presence of outliers with respect to the standard deviation.

It is important to observe that the proper motion obtained previously are characterized by an error which depends on the number of detection of the star and on the quality of the images. Obviously bright stars are easier to detect in each filter therefore the uncertainty on their proper motion will be smaller than that of faint stars. Moreover, the estimate of the uncertainty rely on some assumptions like the fact that stars with the same magnitude share similar photometric properties and consequently the error can be estimated as the medians of the errors of similar stars (see the discussion on the error estimation in section 2.5). As a consequence it may be possible that the estimation of the errors is underestimated especially for faint stars which are the targets with the larger intrinsic uncertainty. Keeping this into account, I can proceed to study the kinematical properties of my system.

The most important quantity used in this work is the so called *Intrinsic dispersion* which by definition is the quadrature difference between the dispersion of the observed quantity and the dispersion of its error:

$$\sigma_{intrinsic} = \sqrt{\sigma_{obs}^2 - \sigma_{err}^2} \tag{3}$$

Physically it should represents the real dispersion net of that contribution due to measurements errors, thus the real dispersion of the quantity.

The quantities in exam in this work are three: the dispersion of proper motion ($\sigma_{intrinsic}$), the dispersion of proper motion along the radial axis (σ_{rad}) and that along the tangential axis (σ_{tan}). In the following when I refer to proper motion without specify an axis I mean that I am studying separately the components along the RA and DEC and then I average them in quadrature. Therefore, to compute the intrinsic dispersion of proper motion I firstly compute the dispersion of the observed motion along RA (i.e. the 68.27^{th} percentile of the proper motion along the RA axis of the group of stars considered) and I do the same for the errors dispersion. I repeat the same for the DEC axis and finally I average them in

quadrature such that:

$$\sigma_{obs} = \sqrt{\frac{\sigma^2_{\mu_\alpha cos(\delta)} + \sigma^2_{\mu_\delta}}{2}} \tag{4}$$

$$\sigma_{err} = \sqrt{\frac{\sigma^2_{ERR\mu_\alpha cos(\delta)} + \sigma^2_{ERR\mu_\delta}}{2}} \tag{5}$$

In the end, the intrinsic dispersion of proper motion will be computed according to equation 3 using the two quantities obtained from equations 4 and 5.

For what concern the radial and tangential axis instead, they are treated as independent and the intrinsic dispersion along these two are computed separately. I made the choice of combining the motion in RA and DEC and leave as independent those along radial and tangential axis because while these latter two are referred to the cluster's center and therefore I can associate a physical meaning to possible trends along these axis, I can not for the RA and DEC axis which are just two lines used as reference for the coordinate system. However, the study of the combination of proper motion along RA and DEC is everything but useless since is the perfect tool to understand if there is a trend of the intrinsic dispersion with magnitude or what kind of sample of stars use and what is the global trend of the components of the system.

It is interesting to deeply analyze how the intrinsic dispersion varies with the radial distance from the center because this allows to have an overview of the radial profile of the system which is the main kinematical property of it.

To compute the radial profile I need to divide the stars in concentric circular coronas (bins). The larger the bin is, the more stars it contains and the more reliable is the value of intrinsic dispersion computed. However, taking large bins means averaging out the properties of the stars in the bin, therefore the larger the bin, the less features will appear in the radial profile. Since there is not a way to decide mathematically the width of the bin, I tried different combinations. After many trials I concluded that, with the data at my disposal, bins of 20arcsec are the best choice.

Since the intrinsic dispersion is a quantity with statistical origin, it strongly depends on the sample used, therefore a reliable estimate of its uncertainty is incredibly difficult. As error of the intrinsic dispersion of proper motion I considered the dispersions of errors normalized to the root of the number of stars from which it was extrapolated. However this method was not robust since a small change in the binning would include a much larger (or smaller) number of stars and consequently the uncertainty strongly fluctuates. Moreover, since the dispersion of the proper motions' errors is very small, especially for RGB stars (which are bright), the errors would be intrinsically very small reflecting in tiny errors dispersions. Since any small change in the sample of reference stars would cause a

variation of the intrinsic dispersion much larger than what predicted by the uncertainties computed this way, I concluded that this method was underestimating them.

I decided then to try two other ways to estimate the errors: the first one consisted in a Monte Carlo procedure, while the second is a Bootstrapping.

- The Monte Carlo procedure used to estimate the errors consisted in select the stars in the bin for which I want to compute the uncertainty on the intrinsic dispersion and, add to their proper motion a fake one obtained from a Gaussian distribution with sigma equal to the error on the proper motion itself, creating this way a fake star with a fake proper motion. The error on this fake proper motion was extracted by the same Gaussian. Once done this for all the stars in the bin, I computed the dispersion of the fake proper motion of the fake stars, the dispersion of their errors, and I subtracted them in quadrature to obtain the intrinsic dispersion of this fake sample. I repeated this 1000 times. As final error on the intrinsic dispersion I took the 68.27^{th} percentile of the distribution of the fake intrinsic dispersion just computed.

- The Bootstrapping procedure is similar to the Monte Carlo one but instead of generating fake stars at each iteration, it simply creates a new sample of real stars. In detail: for the bin for which I am interested in computing the error, I randomly select N stars (where N is the total number of stars in the bin), allowing for the selection of the same stars even multiple times. This way I create a new set of stars which are not fake (the values are the real ones), just rearranged, and I compute the intrinsic dispersion on this sample. I repeated this procedure 1000 times and then, as error on the intrinsic dispersion, I consider the 68.27^{th} percentile of the distribution of intrinsic dispersions just computed.

The errors estimated in these two ways are very similar (the one from bootstrapping is slightly larger) and much larger than the one obtained previously. It is important to point out that the Monte Carlo procedure is reliable just when it is a fact that the errors which I am estimating are gaussian distributed. Since I am not sure of this, I have to reject the estimation from the Monte Carlo procedure and rely on the bootstrap which, however, generally tends to overestimating the errors but, since these are computed on real data just rearranged, it includes any possible source of noise, even those that do not have a Gaussian distribution. The fact that the two estimates of the errors are similar, let me hypothesize that the errors are mostly gaussian distributed (at least in the magnitude range where this discussion was carried out: [-17, -11] in the filter F814W).

3.2.1   Selection of the reference sample

As explained at the beginning of section 3.2, the intrinsic dispersion represents the real spread of the quantity analyzed net of the errors contribution. Since it is an estimator with a statistical basis, the larger the reference sample of stars used, the more this estimator is

reliable in the representation of global quantities. Therefore, in principle, to have the most reliable value, I should compute this estimator on my whole sample, but this averages out possible intrinsic physical differences or may will be dominated by an error component not identified yet.

In addition to the bin size already discussed, another important factor that have to be taken into account in the selection of the sample is the magnitude range from which the stars are taken. As discussed previously, the larger the sample of stars, the more reliable will be the value of the intrinsic dispersion. Therefore, one should in principle include in the sample all the stars independently from their magnitude. While this is in principle true, it does not take into account the fact that faint stars are detected on average in less *epochs* (especially blue filters tends to detect just few faint stars) than the bright ones, moreover, even when they are detected, the uncertainties on their position (relative to the PSF fitting) are intrinsically larger. As a consequence faint stars are characterized by larger errors. Not only the errors are generally larger but also the measured proper motions. Although the variation in the error should be proportional to the variation in proper motion thus they should compensate in the computation of the intrinsic dispersion, this does not happen for vary faint stars. This is why before including in the sample stars of any magnitude I have to check if there is a dependence of the proper motion dispersion from the magnitude.

(a) $\sigma_{\mu_\alpha cos(\delta)}$ as function of the magnitude F814W

(b) $\sigma_{intrinsic}$ as function of the magnitude F814W
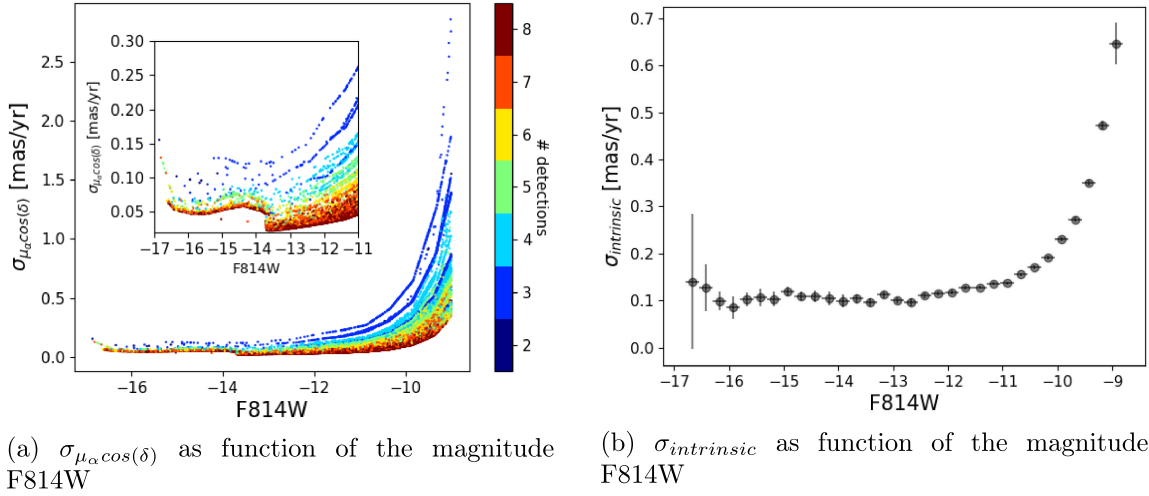
Figure 18: These two plots show respectively the variations of the errors on proper motions (previously referred to as ERRx) as function of the magnitude (figure 18a) and the the dependence of the intrinsic dispersion from the magnitude (figure 18b). In the figure on the left is included a zoom of the region including bright stars. The reference filter used for the magnitudes is always F814W. The colorbar represents the number of detections of the star.

In figure 18a results evident how the errors on the proper motion strongly increase for

faint stars. The minimum errors are at magnitude -13.7 which is the reference value used in the data reduction (see section 2.4) to separate saturated stars from the others. Stars brighter than this value have a larger intrinsic error on the determination of their position precisely because of the saturation, which makes difficult the PSF fitting. For these stars in the optical filters, we used the short exposure images which allowed to have a bit more accurate values, while for UVIS filters this was not possible since all images have almost the same exposure. The very sharp profile of the curve is due to the method used to estimate the error on the position of the star (see section 2.5) which assumes that all stars with the same magnitude should be characterized by almost the same uncertainty. See also how the lower the number of detection is, the larger the error associated to the proper motion.

Referring to figure 18b, where is plotted the intrinsic dispersion of all the stars with a distance from the center of the system between 30 and 110 arcsec (the region where there is the highest number of stars detected), is clear that the intrinsic dispersion of proper motions increases for faint stars. It is not straightforward to understand if this is a physical trend (therefore less luminous, and less massive, stars are on average hotter than the their massive counterpart) or just an artificial one. However, looking at figure 18a I notice that the strongest increase in the errors arises at almost the same magnitude at which the intrinsic dispersion increases. I considered this a sufficiently convincing proof of the fact this sharp rise is due to a systematic which I was not able to remove. The simplest and more precautionary way to proceed with my study is removing from my sample of stars all those stars which starts to have an error compatible with the the proper motion. I rejected from my sample all those stars fainter than magnitude -11 (F814W), which, in a cautious way, is the magnitude below which starts the sharp increase of the errors. This unfortunately means rejecting the majority of my sample of stars.

When I computed the proper motions (section 2.5), I highlighted the fact that not all stars were detected in all the epochs and filters, and those stars detected just in few filters are affected by a large uncertainty. A first check that I made consisted in see if I can consider or not these stars in my sample. On one hand, they are a lot, therefore, including them will largely increase my sample, on the other side they have large uncertainties thus their proper motion may be not as reliable as I wish. To determine if include them or not in the sample, I compare the intrinsic dispersion of proper motions of the stars detected in all the 8 *epochs* with that obtained including stars detected in at least 2 (keeping in mind that to have a minimum accuracy on the values, when I computed the proper motions I asked for stars detected in at least 2 *epochs* with a minimum temporal baseline of 7 years, therefore stars detected just in E1 and E2 are discarded since the temporal baseline is just one year). The result is that shown in figure 19.

As it is clearly visible from figure 19 the trend shown in the two plots is the same but the advantages of including stars not detected in all the 8 *epochs* are evident in particular on the inner and outer parts of the system: including also those stars poorly detected I enlarge the sample and consequently the values obtained are much more reliable since representative

(a) $\sigma_{intrinsic}$ for stars detected just in all the eight filters and epochs

(b) $\sigma_{intrinsic}$ for stars detected also in less epochs
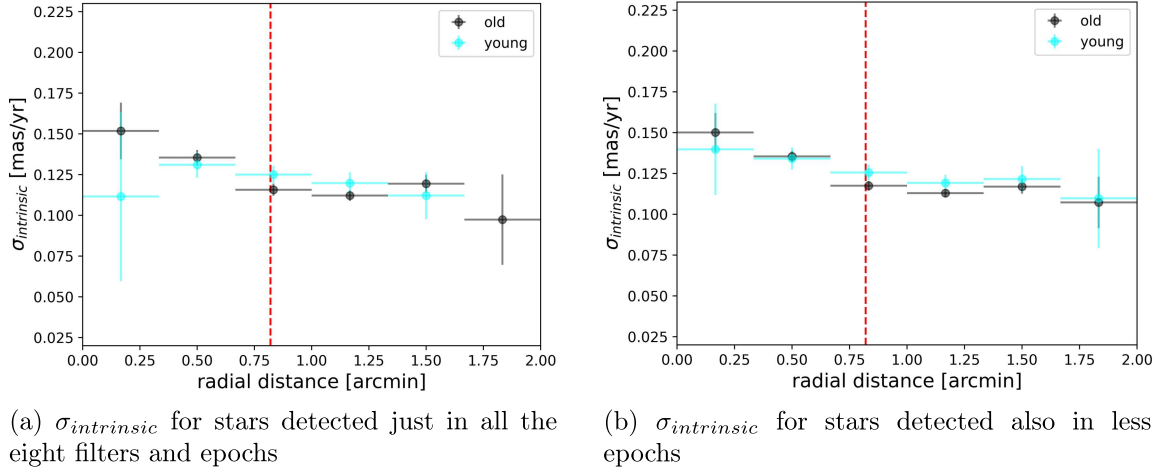
Figure 19: Comparison of the intrinsic dispersion of proper motions computed on a sample including just stars detected in all the 8 *epochs* (figure 19a) and those detected also in less (figure 19b). Error-bars on the intrinsic dispersion are computed with a bootstrap procedure while on the radial distance represent the bin width from which stars were taken to compute the intrinsic dispersion. In both plots black dots represents the old population while cyan dots represents the young one. The dashed red line represents the half light radius of M 54 according to Harris (1996, 2010 edition).

of a larger sample as it is demonstrated from the inner point, which has the uncertainty clearly smaller. Moreover, including also poorly detected stars I add much more samples also in the outer skirts. In fact, while for the young population, in the case of the sample with stars always detected, I do not have any star in the outer bin, I have few detection in the second sample and this allows me to analyze also that region (even if stars are too few to infer strong conclusions).

Stars of the old population detected in all the 8 *epochs* are 3875 while in the other sample are 6149; for the young population I have 1146 stars detected in the first sample and 2048 in the other. In both cases the number of stars in the sample including also the poorly detected ones is almost doubled.

The brighter limit of the magnitude range used for this discussion is fixed according to the brightest star present in the sample of stars detected in all the 8 *epochs* (-16.5mag) and I kept it also for the other plot but, including also stars detected in less *epochs* the brighter limit would be -17, therefore using the second data-set allows also to include stars in a larger magnitude range.

Looking at these plots and after this qualitative discussion, I concluded that including stars poorly detected is the best choice: the possibility of almost doubling the sample of stars at my disposal allows to take stronger conclusions on which really are the global kine-

matical properties of the system. Since the intrinsic dispersion averages out the properties over the large sample, even if some of the poorly detected stars have possibly non reliable proper motions, these would be the minority and therefore give a negligible contribution. I decided that for the rest of the analysis I will include in my sample of stars also those poorly detected.

In the rest of the work I will use stars detected in at least two *epochs* with a temporal baseline of at least 7 years. I will restrict my sample to the magnitude range [-17, -11] in the filter F814W and stars are divided in the old and young populations as described in section 3.1. For what concern the sub-populations of the old population, those identified from the RGB are in the magnitude range [-17, -12] while those identified in the SGB are in the range [-11.9, -11.3]. The majority of stars identified with HST populate the MSs of the system but are also those characterized by the largest errors (are fainter than mag. -11) therefore I have to reject them all .

This process left me with a total of 6149 stars relative to the old population in the magnitude range [-17, -11] and 2048 relative to the young population in the same range of magnitudes.

4 Results

In the following, I present the main results on the internal kinematics of stellar populations identified in section 3. This section is organized as follows: in section 4.1 I discuss the spatial distributions of stars in the Sagittarius dwarf spheroidal galaxy (Sgr dSph) and in the distinct populations within its nuclear GC, M 54. Section 4.2 compares the internal kinematics of the galaxy and the cluster, while in section 4.3 is studied the anisotropy of the population and is provided the first geometric measurement of the distance of M 54 combining the proper-motion dispersion derived in this thesis (an angular quantity), with the radial-velocity dispersion (a linear quantity) from Alfaro-Cuello et al. (2020). The kinematics of the distinct stellar populations of M 54 are discussed in section 4.4. The summary of the results and a discussion follow in section 4.5.

4.1 Spatial distributions of stellar populations in M 54 and in the Sgr dSph

To investigate the distribution of stars on the plane of the sky, I exploit the same method adopted in section 2.6 for determining the center of the populations and computing the radial and tangential proper motions . Specifically, I analyze the contours of the coordinate distributions of stars in the distinct populations.

To carry out a study on the morphology of each stellar population, I analyze stars with high-precision magnitude measurements based on the photometric criteria of selection made in section 3.1. As a consequence, the innermost regions are strongly affected by incompleteness. Indeed, it is not possible to derive high-quality photometry in the crowded cluster core. To increase the sample of analyzed stars, I included stars without proper-motion determinations and faint stars that, due to the large astrometric uncertainties, have been not included in the proper-motion study[8]

A visual inspection at the contour plots of Figure 20 reveals that the old and young populations exhibit different spatial distributions. While the old population roughly follows circular symmetry, the young stars are distributed along elongated ellipses.

The evidence that the two populations have different spatial distributions is confirmed by the fact that the old population is fitted by an ellipse with eccentricity (defined as $\epsilon = \sqrt{1 - \left(\frac{b}{a}\right)^2}$ with a and b respectively the semi-major and semi-minor axis) $\epsilon = 0.08 \pm 0.04$ while the young population is consistent with an eccentricity $\epsilon = 0.28 \pm 0.05$. The uncertainties are estimated by means of bootstrapping, with 1,000 replacements of the original sample. Since HST's field of view is squared, boundary effects may affect the estimates of eccentricity of the populations. However, both the estimates on the young and on the old populations are affected by the same bias, therefore the relative differences have to be intrinsic and not artifacts.

---

[8]30,501 are the stars considered as member of the old population to study its morphology while for the young population are 3,516.
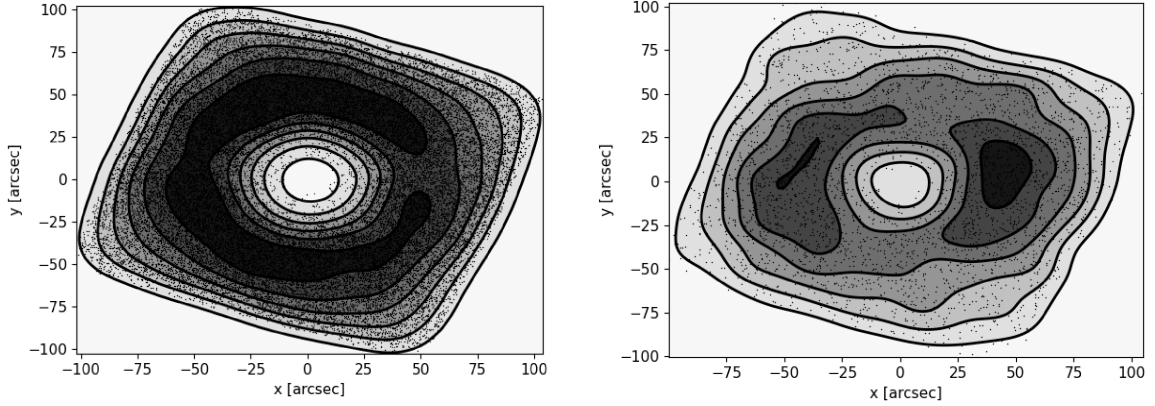
(a) Space distribution of stars in the old population.

(b) Space distribution of stars in the young population.

Figure 20: Comparison between the contour plots of the old (left) and young (right) populations. Stars of each populations are indicated by dots, while the contours are represented with black lines. The gray levels are indicative of stellar density, with the highest stellar density indicated by black colors. Contours are smoothed with a bandwidth parameter set to 0.2.

The different spatial distributions of the young and the old population corroborates the evidence that they are distinct stellar systems. The eccentricity of the old population is consistent with zero, at $\sim$2-σ level. Hence its stars follow a nearly-circular distribution on the plane of the sky, in close analogy with what is observed in the majority of GCs. On the contrary, the flat distribution of stars in the young population is typical of a galaxy.

Intriguingly, the centers of the young and the old populations, which have been derived by using the procedure of Section 2.6, are consistent with each other, and this conclusion is significant at $\sim 1\sigma$-level. In detail, having shifted all the system with respect to the center of the old population, this latter lays in (0.0, 0.0) $\pm$ (0.9, 0.2) while the young population's center lays in (2.3, 2.5) $\pm$ (20.4, 3.7) [9]. The larger uncertainties on the center of the young population are both due to the lower number of members respect to the old, and to the non-circular symmetry.

This finding, together with the evidence that the two populations share the same average proper motions (see section 2.5), demonstrates that the young and the old populations are not distinct stellar systems on the same line of sight but are mixed in the center of the Sgr dSph.

---

[9]The values in brackets represents the coordinate in RA and DEC measured in arc-seconds

(a) Stars belonging to population 1G

(b) Stars belonging to population 2G

(c) Stars belonging to the Anomalous population
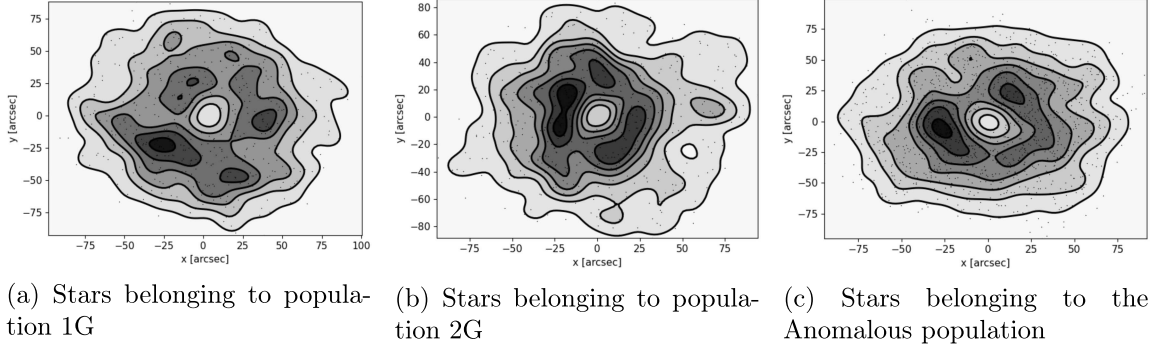
Figure 21: Comparison of the contour plots of the sub-populations within M 54 identified through the Chromosome Map of the RGB. Stars of each populations are indicated by dots, while the contours are represented with black lines. The gray levels are indicative of stellar density, with the highest stellar density indicated by black colors. Contours are smoothed with a bandwidth parameter set to 0.2.

4.1.1   Spatial distributions of multiple populations within M 54

To investigate the distributions of stellar populations within M 54, I extended the procedure discussed in the previous sections to the groups of 1G, 2G and Anomalous stars identified from the Chromosome Map of the RGB and shown in Figure 21.

It results that the three stellar populations[10] share the same eccentricity within one-σ. Specifically the eccentricity of 1G stars is $\epsilon = 0.31 \pm 0.11$, whereas for the 2G and the Anomalous populations, I find 0.20 ± 0.10 and 0.27 ± 0.09, respectively. As expected, due to the smaller number of studied stars, the uncertainties associated to the eccentricity values of the stellar populations within M 54 are larger than those of the old and the young populations.

Finally, I analyze the radial distributions of stellar populations in M 54 and in the Sgr dSph by means of their cumulative distributions. Due to the low completeness, I excluded stars within 20 arcsec from the cluster center.

Results are illustrated in Figure 22, where I show that 2G stars are more-centrally concentrated than the 1G. Intriguingly, Anomalous stars follow similar radial distribution as the 2G.

The spatial distributions of multiple populations in GCs has been widely used to constrain the formation scenarios of multiple populations. Indeed the present-day distributions of 1G and 2G stars, in stellar systems that are not entirely relaxed, preserve fossil information about their initial distribution. The fact that 2G stars are most-centrally concentrated is consistent with the hypothesis that 2G stars of M 54 formed in the innermost cluster

---

[10]For the study of the morphology I considered respectively 564 stars as part of 1G, 584 members of 2G and 1282 for the Anomalous population
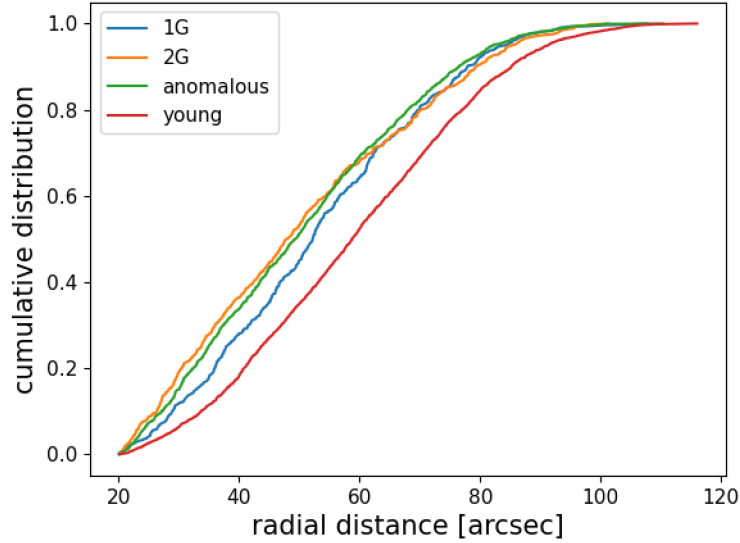
Figure 22: This plot shows the cumulative distribution of stars belonging to different populations as function of the radial distance from the center of the cluster identified as explained in section 2.6.

regions, possibly as a consequence of cooling flow processes. The evidence of a more centrally concentrated 2G is not a peculiarity of M 54 but has been observed in some other massive GCs, including 47 Tuc, ω Cen, M 3 and NGC 2808 (e.g. Sollima et al., 2007; Bellini et al., 2009; Milone et al., 2012; Cordero et al., 2014; Dondoglio et al., 2021). These results suggests that the 2G of these clusters have experienced similar formation histories. It is worth noticing that 1G and 2G stars in low mass GCs share the same radial distribution (e.g. Milone et al., 2009; Milone et al., 2019; Dondoglio et al., 2021 and references therein).

Intriguingly, the Anomalous population follows the same trend of the 2G, thus suggesting a common origin for 2G and Anomalous stars.

To validate this result I performed a Kolmogorov-Smirnov test between each couple of populations. The test confirms (with a p-value=0.54) that just the 2G and the Anomalous population share the same radial distribution; for the other couples of populations tests give p-values below 0.01 allowing for the rejection of the null hypothesis that the two populations tested share the same spatial distribution.

For completeness, I show the cumulative distributions of stars in the young population. As expected, the stars of the galaxy are less concentrated than stars in the stellar populations within M 54.

4.2 Kinematics of the old and the young populations

The main results on the kinematics are illustrated in Figure 23, where I show the intrinsic velocity dispersions for the old and young populations, measured along the radial and tangential axis, against the radial distance from the cluster center. The red vertical lines superimposed on both panels of Figure 23 mark the half-light radius of M 54 and correspond to 49.2 arcsec (Harris, 1996, 2010 edition). In the following, I use this line to separate the *inner region*, which hosts stars located within the half-light radius, from the *central region*, which ranges from one to two half-light radii, and the *outer region* composed of stars outside two half-light radii.

(a) Intrinsic dispersion along the radial axis (b) Intrinsic dispersion along the tangential axis
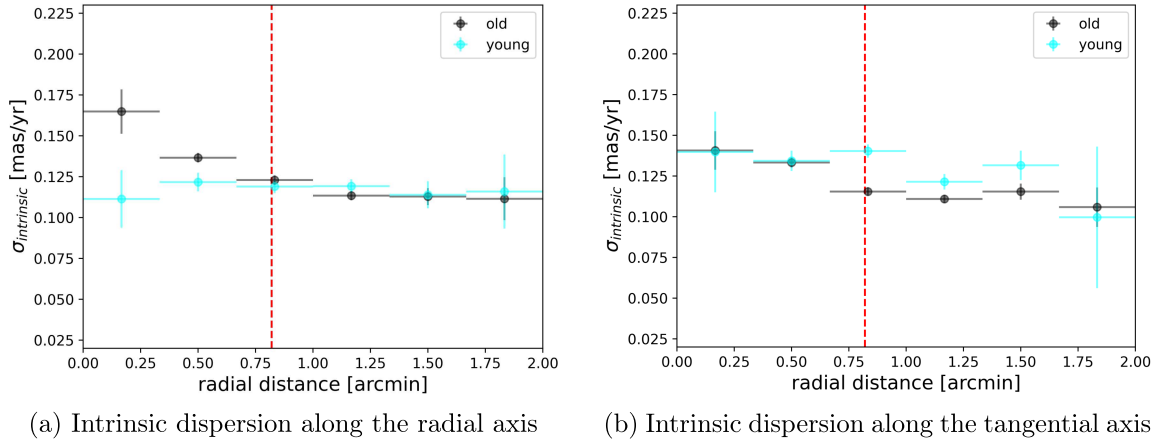
Figure 23: Plots of the intrinsic dispersion of proper motion along the radial and tangential axis. Error-bars on the intrinsic dispersion are computed with a bootstrap procedure while on the radial distance represent the bin width from which stars were taken to compute the intrinsic dispersion. The dashed vertical line represents the half light radius (49.2 arcsec) of the cluster according to Harris (1996, 2010 edition).

Clearly, the velocity dispersion of old stars depends on the radial distance. It approaches its maximum value ($\sigma_{\mathrm{intrinsic}} \sim 0.15$ mas yr^{-1}) in the cluster center and steadily declines to $\sigma_{\mathrm{intrinsic}} \sim 0.11$ mas yr^{-1} in the *outer region*. Qualitatively, the observed trend is consistent with what is expected from a Plummer profile, where stars are kinematically hotter towards the center of the stellar system. The velocity-dispersion distributions along the radial and tangential axis follow similar trends although the latter seems to exhibit a less pronounced decline. The motions along these two different directions will be further analyzed in section 4.3 to investigate possible anisotropies.

On the contrary, the young population exhibits nearly flat velocity-dispersion distributions. Specifically, the probability of constant velocity dispersions are 0.95 and 0.62 along the radial and the tangential axis, respectively. I refer to Appendix A.1 for details on the procedure used to estimate these probabilities. The finding of a flat distribution is consis-

59

tent with the hypothesis that the young population is associated with a stellar system that extends over a wide field of view. In this case, it would be no possible to appreciate any velocity-dispersion variation within the small ($\sim 2 \times 2$ square arcmin) HST field of view.

Intriguingly, the young and the old populations share similar velocity dispersions within 0.05 mas yr^{-1}. The central region, where young-population stars seem hotter than the old population ones seems a remarkable exception, which could indicate that the old and the young populations have distinct kinematics[11].

Intriguingly, along the tangential axis, young-populations stars at one half-light radius, are kinematically hotter than old-population stars by more than 3σ. The significance level decreases going outwards. This fact may indicate that Sgr dwarf stars have different rotation with respect to the old population.

To investigate whether the conclusions are affected by the estimate of observational errors, I noticed that the ratio between the proper-motion dispersions of the old and the young population is an efficient quantity to investigate their relative kinematics. Indeed, as discussed in Sections 2 and 3, proper motions of stars with similar luminosity share similar errors. Hence, their ratio is poorly affected by observational uncertainties[12]. The ratio $\sigma_{obs,old}$ over $\sigma_{obs,young}$ along the radial and tangential axis is that shown in figure 24. Clearly, this figure confirms previous conclusions that i) the old population is hotter than the young one in the inner region along the radial axis and ii) the young population has higher velocity dispersion along the tangential axis in the central region, possibly due to different rotation patterns.

4.3 Anisotropy

In this subsection I investigate possible deviations from isotropic motion of the old and the young populations. To do this, I exploit the anisotropy parameter, which is defined as

$$K = \frac{\sigma_{tan}}{\sigma_{rad}} - 1 \qquad (6)$$

Hence, the isotropic motion correspond to K=0. Positive and negative values of K indicate deviations from isotropic motions in the tangential and radial direction, respectively.

The anisotropy parameter of the old and of the young population is shown in figure 25 as a function of the radial distance from the cluster center. The old population seems consistent with an isotropic stellar system, although the large scatter prevents me from firm conclusion. On the contrary, the young population is consistent with significant deviation from isotropy, as expected for a fast-rotating stellar system.

---

[11]The results discussed in this section are obtained from the procedure described in section 3. To demonstrate the conclusions do not depend on the method, in the Appendix A.2 I estimate the velocity distributions by adopting a different approach based on a Monte Carlo analysis.

[12]For details on the propagation of the errors over the ratio operation I refer to Appendix A.3

(a) Ratio of the observed dispersions along the radial axis

(b) Ratio of the observed dispersions along the tangential axis
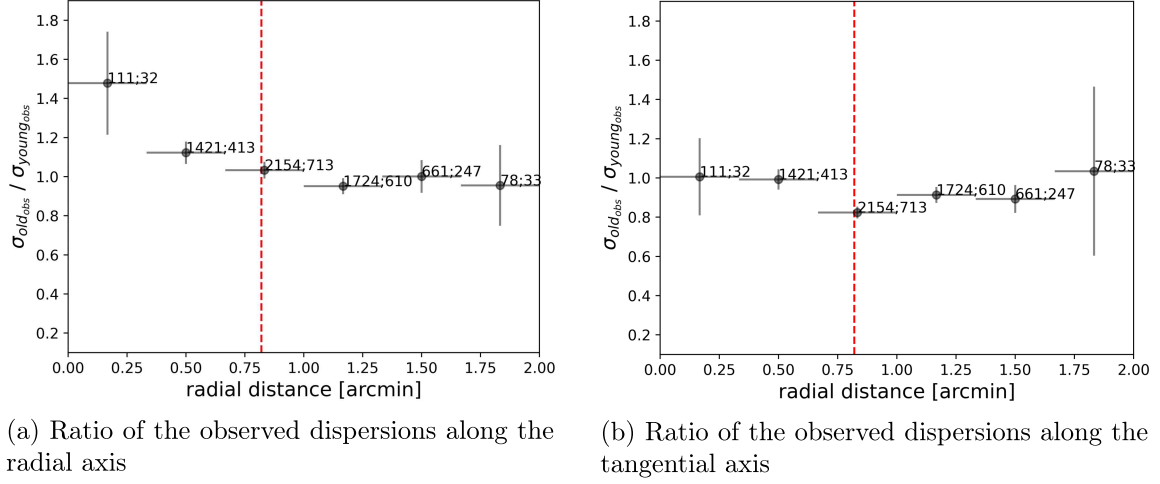
Figure 24: Ratio between the observed velocity dispersions of the old population over the young one along the radial (left) and the tangential axis (right). Error-bars associated to each point are derived from equation 9 while the segments on the horizontal axis mark the extension of the corresponding radial bin. For each point are indicated the number of stars respectively of the old and young population in that bin.

4.3.1 Geometric distance of M 54

The possibility that the old population exhibits isotropic motions in the innermost cluster region, provides the unique opportunity to measure its geometric distance by comparing the proper motion dispersion (an angular quantity) with the radial-velocity dispersion (a linear quantity).

Specifically, I can use the equation

$$d[pc] = \frac{v_{los}[km/s]}{4.74\,\mu[arcsec/yr]} \tag{7}$$

where d is the distance, v_{los} is the velocity dispersion along the line of sight, μ is the proper motion dispersion. By adopting the profile of the line of sight velocity dispersion of stars within two arcmin by Alfaro-Cuello et al. (2020) and the profile of the proper motion dispersions inferred in this work, I find a distance of 22.2±1.8 kpc, which differs by 2.4-σ from the value provided by Harris (1996, 2010 edition) (26.5 kpc) based on isochrone fitting.

The errors on the distance measurement was estimated as standard deviation of all the distance estimates obtained comparing the dispersions at increasing radial distance.

As an exercise, I extended the analysis to the young population and it results a distance of 25.3±2.2 kpc, which is in agreement at ∼1-σ level with the distance of M 54. Nevertheless, the fact that the young population exhibit anisotropic proper motions prevents from a reliable distance determination.

(a) Anisotropy parameter of the old population function of the radial distance

(b) Anisotropy parameter of the young population function of the radial distance
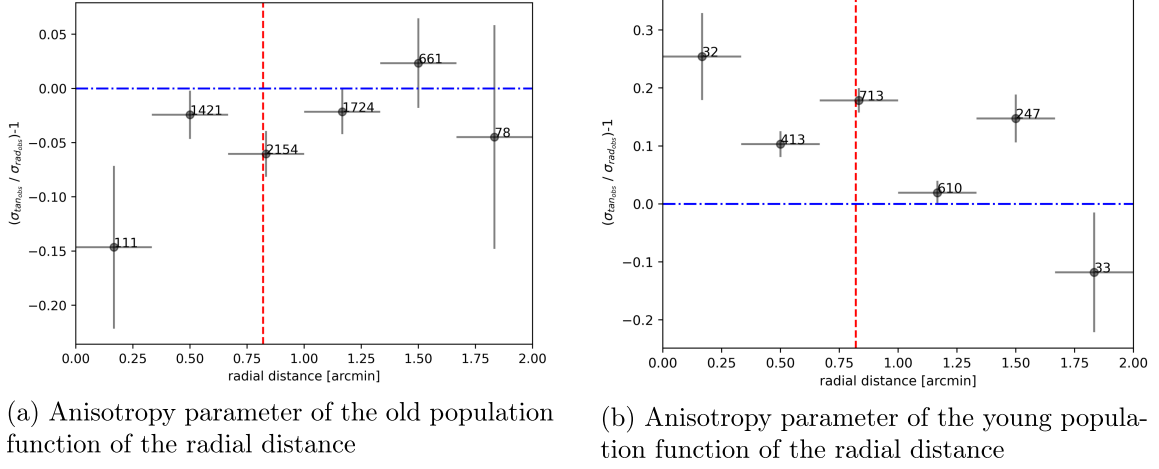
Figure 25: In this figure are reported the trend of the anisotropy parameter as function of the radial distance from the center of the cluster respectively for the old population (figure 25a) and for the young one (figure 25b). Error-bars on the anisotrpy parameter are computed according to equation 9 while on the radial distance represent the bin width from which stars were taken to compute the values of the intrinsic dispersion.The blue dashed line represents the isotropy while the vertical dashed red one represents one half-light radius. For each point are indicated the number of stars respectively of the old and young population in that bin.

For completeness, I derived the distance by adopting the estimates of proper motion dispersion along various directions. Results are provided in Table 2.

	OLD	YOUNG
AVERAGE (RA-DEC)	$22.2 \pm 1.8\ kpc$	$25.3 \pm 2.2\ kpc$
RADIAL	$21.7 \pm 1.7\ kpc$	$27.0 \pm 1.9\ kpc$
TANGENTIAL	$22.8 \pm 1.9\ kpc$	$24.8 \pm 2.1\ kpc$

Table 2: In this table are collected the estimates of the distances obtained from the analysis of the tangential and radial axis of the old and young populations. *Average (RA-DEC)* refers to the dispersion of proper motion computed averaging the dispersion along the RA and DEC axis as explained in section 3.2 and according to equations 4 and 5.

Values obtained per each population are compatible within one standard deviation. Estimates of the distance obtained from the old population are in agreement with that reported in Harris (1996, 2010 edition) of 26.5 *kpc* at less than 3-σ level while from the young population at less than 1-σ level.

To have a smaller uncertainty on the distance, I need more refined values of both the intrinsic dispersions on the line of sight and on the plane of the sky.

4.4   Kinematics of multiple stellar populations within M 54

In addition to study the kinematics of the old and the young population, this work aims to shed light on the kinematics of the sub-populations detected from the Chromosome Map of the RGB and from the splitted SGB of the old population.

The identification of the sub-populations was made in section 3.1: there I highlight the so called 1G, 2G, the Anomalous population and the Bright and Faint SGBs.

The comparison between the intrinsic dispersion of proper motions (obtained averaging the dispersion of proper motions along the RA and DEC axis) shows that closer to the center of the system, in the inner region, the 1G and 2G populations are the hottest ones with a central intrinsic dispersion respectively of $\sigma_{0;1G} = 0.156 \pm 0.036\,mas\ yr^{-1}$ and $\sigma_{0;2G} = 0.166 \pm 0.020\,mas\ yr^{-1}$. The Anomalous and the young population have a central intrinsic dispersion respectively of $\sigma_{0;young} = 0.140 \pm 0.027\,mas\ yr^{-1}$ and $\sigma_{0;anomalous} = 0.134 \pm 0.018\,mas\ yr^{-1}$. Intriguingly the anomalous population has a central dispersion that is not compatible within 1-σ neither to that of the 1G nor that of the 2G.

The 1G and the Anomalous population have a similar trend on the radial axis (Table 3) and in the outskirts assume a value of the intrinsic dispersion comparable to that of the young one while the 2G is colder in the outskirts.

On the tangential axis instead (Table 4), in the inner region the three populations are characterized by a comparable intrinsic dispersion while, outer one half-light radius, the Anomalous population shows a decreasing trend similar to the 2G but not to the 1G which tends to be hotter. Both the 2G and the Anomalous population on the tangential axis are globally colder than the young population suggesting they are rotating at a lower speed. The 1G instead, outer one half-light radius shows an intrinsic dispersion comparable within one standard deviation to that of the young population.

To validate these results I tried to restrict the populations: I divided the 1G in two sub-populations namely *1G-classic* which contains 1G stars with a $\Delta_{F275W-F814W} < -0.21$ and *1G-anomalous* which contains the rest of the 1G stars. I also roughly removed from the Anomalous populations the stars which are in the center of the Chromosome Map with the aim of reducing the contamination. Although rejecting few stars and dividing the 1G in two sub-populations reduces the number of samples, it allows me to verify if possibly part of the population that I called 1G was instead part of the Anomalous.

I found that the 1G-anomalous is compatible within one standard deviation with all the other populations. The same discussion applies to 1G-classic.

I checked then the kinematics of the populations identified as Bright-SGB and Faint-SGB. These two show a comparable intrinsic dispersion at 1-σ level as shown in figure 26.

I compared these with the sub-populations identified from the Chromosome Map of the
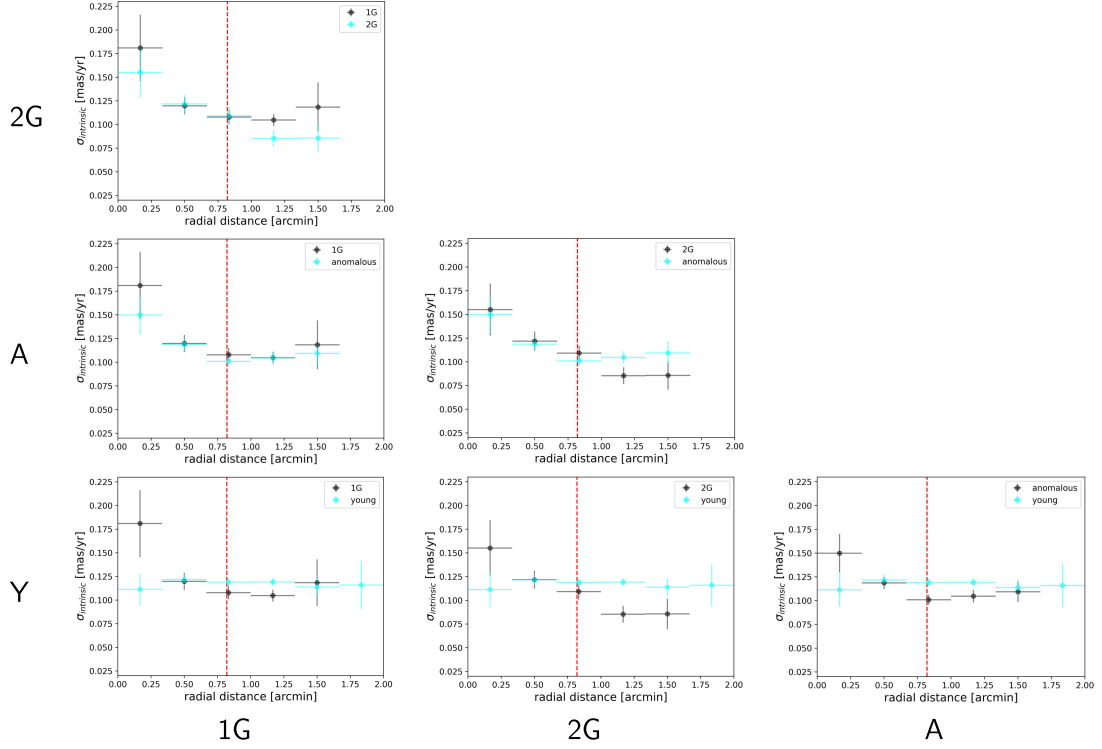
Table 3: Intrinsic dispersion along the radial axis of the young population (Y) and the different populations identified from the RGB: 1G, 2G, A (Anomalous)

RGB. The Bright-SGB shows a radial intrinsic dispersion compatible with all the RGB populations at 2-σ level. Along the tangential axis the Anomalous population is globally colder than the Bright SGB by more than 2-σ.

The Faint-SGB on both the radial and tangential axis is compatible within 1.5-σ (with some outliers) with all the populations identified from the RGB.

According to photometry I expected to find a clear relation between the Bright-SGB and the 2G and between the Faint-SGB and the Anomalous population since these seem to be their natural extensions. However, the results obtained in this work do not allow to recover a clear kinematical counterpart at a sufficient significance level.

The anisotropy parameter of each population identified from the RGB is scattered around zero meaning that all the populations are characterized by an isotropic motion. The same result is found for the populations identified from the SGB.
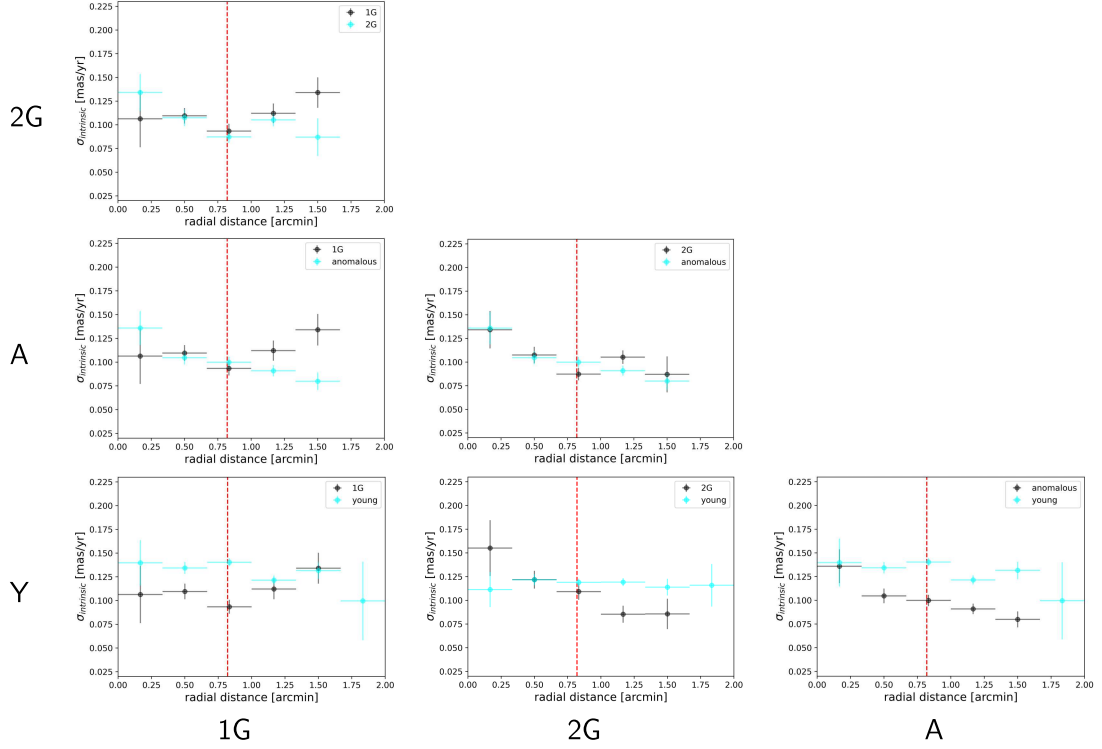
Table 4: Intrinsic dispersion along the tangential axis of the young population (Y) and the different populations identified from the RGB: 1G, 2G, A (Anomalous).

4.5 Summary and Discussion

I have analyzed archive images collected through the F275W, F336W, F438W filters of UVIS/WFC3 and the F606W and F814W filters of WFC/ACS on board *HST*. I derived high-precision photometry and astrometry by exploiting the method and the computer programs developed by Anderson and collaborators and based on the effective PSF. Available images have been collected during a period of eight years, ranging from 2006 to 2014, thus allowing the determination of relative proper motions.

These data are used to generate a catalogue of multi-band photometry and high-quality proper motion determinations of ∼30,000 stars associated to the system composed of M 54 and the Sagittarius galaxy.

Based on CMDs build with appropriate combinations of UV and optical filters I disentangled stars of the old (≃ 13 Gyr) and young population, which are mostly composed of stars in M 54 and in the galaxy, respectively. By combining information from photometry and proper motions, I explored the relative kinematics of these stellar populations on the plane of the sky. The main results can be summarized as follows:

(a) Intrinsic dispersion along the radial axis (b) Intrinsic dispersion along the tangential axis
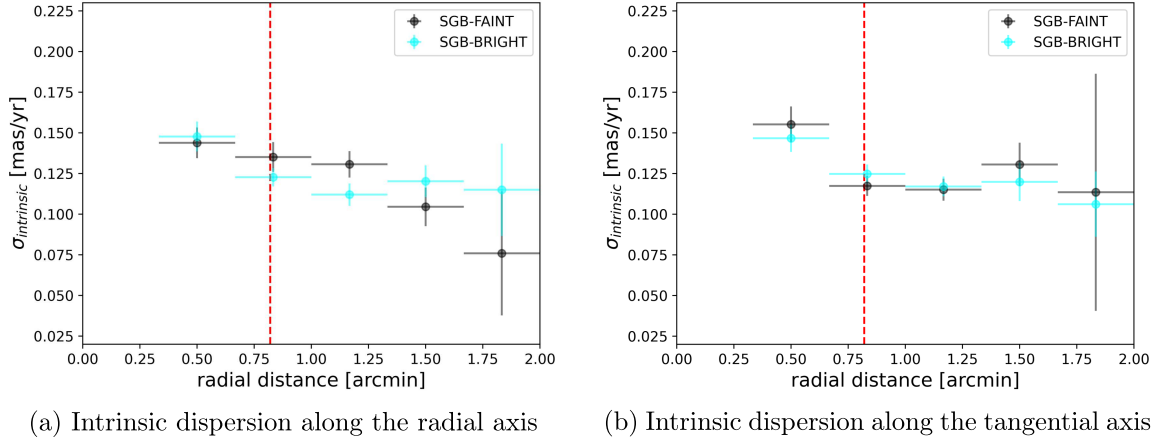
Figure 26: Plots of the intrinsic dispersion of proper motion along the radial and tangential axis of the Bright and Faint SGBs. Error-bars on the intrinsic dispersion are computed with a bootstrap procedure while on the radial distance represent the bin width from which stars were taken to compute the intrinsic dispersion. The dashed vertical line represents the half light radius (49.2 arcsec) of the cluster according to Harris (1996, 2010 edition).

- The old and the young population share the same centers and the same mean motions on the plane of the sky.

- The old and young populations exhibit different spatial distributions. The old population is roughly circular, in close analogy with the majority of GCs, while the young one is flattened and is consistent with an ellipse with eccentricity $\epsilon = 0.28 \pm 0.05$, which is a common feature of dwarf galaxies. As expected, the old population, which is associated to M 54, is more centrally concentrated than the young population (assciated with the galaxy).

- I measured for the first time the velocity-dispersion profiles of the young and the old population on the plane of the sky. The velocity dispersion of the old population ranges from ~ 0.15 mas yr^{-1} in the cluster center to ~ 0.11 mas yr^{-1} at radial distance of about 2.0 arcmin. The cluster is consistent with having isotropic motions.

- On the contrary, the velocity dispersion of the young population is nearly constant (~ 0.12 mas yr^{-1}) both on the radial axis (i.d. towards the center) and the tangential axis. The motion exhibits significant departures from isotropy and indicates that the young population is strongly affected by rotation.

- By assuming that the old population has isotropic motions, I combined its proper motion dispersion with the line of sight velocity dispersion provided by Alfaro-Cuello et al. (2020) to derive the first geometric estimate of the cluster distance. I obtain

a distance of $22.2 \pm 1.8\,kpc$, which is compatible at 2.4-σ with the value of 26.5 kpc reported in Harris (1996, 2010 edition) based on isochrone fitting.

To investigate the kinematics of multiple populations within the GC M 54, I started exploiting the diagram dubbed Chromosome Map to identify three main stellar populations along the RGB of M 54, namely 1G, 2G and Anomalous population. Based on their position on the Chromosome Map, 1G stars have the same chemical composition as halo field stars with the same metallicity, while 2G stars have the same metallicity as the 1G but are enhanced in He, N, Na and depleted in C and O. The anomalous population is composed of stars enhanced in iron content, and is present in a small fraction of about 17% of studied GCs, named Type II. In addition to the multiple populations along the RGB, I find that the SGB of M 54 is clearly split, thus allowing to identify a faint and a bright SGB. The main results on multiple populations in M 54 include:

- I investigate the radial distribution of multiple populations finding that Anomalous population shares the same radial distribution as the 2G. Both the Anomalous population and the 2G are more centrally concentrated than the 1G.

- I derived the velocity-dispersion profiles for each population and I find that the 2G and the Anomalous population follow similar trends, with the dispersion ranging from ~ 0.15 mas yr^{-1} towards the center to ~ 0.09 mas yr^{-1} at radial distance of about 1.5 arcmin. On the contrary, the 1G seems consistent with a flatter velocity-dispersion distribution. Intriguingly, the velocity-dispersion profiles of all populations within M 54 significantly differ from the velocity profile of the young population.

- Finally, I measured the velocity dispersion profiles of the Bright-SGB, which is compatible at 1-σ level with that of the Faint-SGB but differs from the profile of the young population.

The fact that none of the stellar populations within M 54 share the same morphology and kinematic properties as young-population stars demonstrates that multiple stellar populations within the GC have different formation history than those in the galaxy.

On the other side, the evidence that multiple populations within M 54 have different radial distribution demonstrates that this GC is not a relaxed stellar systems. Hence, the present day spatial distribution and kinematics would retain information on the formation process of its multiple populations.

The evidence that 2G stars are more centrally concentrated than the 1G is not a peculiarity of M 54 but is a common feature of several massive GCs, which suggests a common origin for 2G stars in M 54 and in the other GCs. Specifically, the high concentration of 2G stars is considered the signature that the second generation formed in a high-density environment in the cluster center, possibly as the consequence of cooling flow.

Results on the Anomalous population may provide new insights on the formation history of type II GCs. The notion is still entertained on whether the metal-rich stars are the

product of a merger between sub-clusters or their high metallicity is due to pollution from supernovae from a previous generation. In the latter case, the proto-GC would have been significantly more massive at formation, to retain the fast ejecta from supernovae.

The evidence that the Anomalous population shares the same properties as the 2G may suggest that merging process is unlikely responsible for the origin of 2G stars. On the contrary, it is tempting to suggest that Anomalous stars could form via cooling flow, in close analogy with what occurred for the 2G. If this phenomenon occurred when M 54 was already in the nucleus of the Sagittarius dwarf, the strong gravitational field due to the galaxy may have contributed to retain supernova ejecta, thus mitigating the mass-budget problem. If this scenario is correct, it is tempting to speculate that Type II GCs are nuclei of tidally disrupted dwarf galaxies.

4.6 Future perspectives

All the results presented in this thesis can be further improved with new observations especially in the optical or near-IR filters which grant more detection with a larger accuracy therefore allowing for better estimates of the proper motions. These can be achieved by HST in future GO or with the upcoming James Webb Space Telescope (JWST) which, with its larger mirror and being designed to maximize its performances in the near-IR, would be the best candidate. To improve the quality of proper motions is sufficient to extend the temporal baseline taking new images of the system. The optical and near-IR filters are those with the larger number of detections and with the larger accuracy, this is why they are the best ones to pursue the aim of getting more accurate proper motions.

Alternatively data from Gaia EDR3 (van Leeuwen et al., 2021; González-Núñez et al., 2021) would allow to extend this work much further than 2 arc-minutes from the center of the system using absolute proper motions unveiling also the rotational profile of the system. However, as a drawback, Gaia resolution does not allow to detect as many stars as HST or JWST in particular in crowded and far regions as the system $M\,54 + Sgr$. This makes more difficult a statistical discussion on global properties of the system. Up to now, using Gaia to get proper motions of the stars within the first 2 arc-minutes of the system is not possible since it is not able to clearly disentangle and follow many stars. In the EDR3, in the same field of HST, are catalogued just few bright sources and these are not enough to grant a significant discussion on the kinematics of the system (this issue may be resolved by future data releases). This is why Gaia would be more useful to analyze the outskirts of the system which are not covered by the small field of HST.

Other kinematical features of this system can be investigated combining the proper motions obtained in this work with the radial velocities obtained by the Multi-Unit Spectroscopic Explorer (MUSE) at the Very Large Telescope (VLT) and presented for the first time in Alfaro-Cuello et al. (2019). The combination of these two data-set would unveil the three dimensional motion of the stars in the system allowing for a much deeper understanding of the kinematics of the different populations.

A Appendices

A.1 Validation of the constant velocity dispersion

To verify that the intrinsic dispersion of the young population is effectively compatible to a constant I checked the hypothesis with a Monte Carlo analysis. The procedure was implemented this way:

- For a fixed population compute the weighted average of the intrinsic dispersion.

- Create a sample of N points (where N is the number of intrinsic dispersion that you have computed) and as abscissa assign them the same distance at which was computed the intrinsic dispersion, as ordinate the weighted average and as error the same error of the measure of the intrinsic dispersion at that distance. This way all these new reference points follow a straight line with null slope and intercept equal to the weighted average.

- Fit these reference points to a straight line in order to get the uncertainty on the the reference slope (which, for the procedure adopted to create the points, must be zero).

- Now for each measure of the intrinsic dispersion sample a value from a Gaussian distribution centered in zero and with standard deviation equal to the standard deviation of the original point. Add this value to the original one of the intrinsic dispersion at that distance. This way I am sampling N points Gaussian distributed according to the uncertainties of the measurements. Fitting these N points to a straight line I get an estimate of the slope which can be compared to the reference one.

- Repeat the previous passage multiple times and, assuming a frequentist approach, the probability that the data are compatible with a constant equal to their weighted average is given by the number of times the Monte Carlo's slope was compatible with the reference one, divided by the total number of trials (which in this work was set to 1000).

Using this procedure I was able to confirm that the intrinsic dispersion of the young population along the radial axis is compatible to a constant equal to $0.120 \pm 0.002 \, mas \, yr^{-1}$ with a probability of 95%. Its tangential axis instead is compatible with a constant equal to $0.150 \pm 0.009 \, mas \, yr^{-1}$ with a probability of 62%.

The constants obtained from the two axis are not compatible within one standard deviation and this suggests the presence of a small anisotropy. The presence of anisotropies will be further studied in section 4.3.

A.2 Monte Carlo as validation of the results

To validate the results obtained studying the kinematics of the old and young populations, I perfomed a Monte Carlo analysis to compute the intrinsic velocity-dispersion.

For the Monte Carlo analysis I created N fake-stars with a Gaussian error randomly sampled from the errors of the real-stars. I summed to them different values of intrinsic proper motion and I compared this sum with the observed dispersion. This way, the value of intrinsic dispersion that summed with the dispersion of the errors best fits the observed dispersion, is associated to the most reliable value of intrinsic dispersion. This is true in the assumption that the errors are Gaussian distributed. After few trials I noticed that this procedure strongly suffer low statistic which is the case of the inner and outer regions of the system $M\,54 + Sgr$. To solve this puzzle I considered a slightly different procedure: instead of assigning to each of the N fake-stars a random error sampled from a Gaussian built on the error of a randomly selected real-star, I created N random copies of the real-stars assigning them the same errors of the real star randomly selected. This way the procedure suffer less the low statistic and allows to have a better estimate of the intrinsic dispersion of proper motion.

More in detail, the steps in which the procedure is articulated are:

- For a fixed population, divide the stars in bins of increasing radial distance.

- For each bin generate N fake-stars as copies of randomly selected real-stars in the bin. This way each fake star will be characterized by an error on the proper motion which is the same of a real-star. For this work I selected N=10000. At the end of this step I have a list of fake-stars with the same distribution of errors of the reals-stars in the bin but enlarged in number. Compute the 68.27^{th} percentile as estimator of the dispersion of the errors.

- Sum in quadrature to this value a guess of the dispersion of the intrinsic proper motion creating this way a fake dispersion of observed proper motion. Compute the square residuals of this from the real dispersion of observed proper motion.

- Repeat this last passage K times changing at each iteration the guess value of the intrinsic proper motion. For this work I repeated this step K=5000 times changing the guess value by the maximum proper motion observed in the sample divided by K.

- Even if conceptually I can take the value of intrinsic proper motion that give rise to the lowest residual, since the results of the simulations undergo the stochastic fluctuations intrinsic of the Monte Carlo procedure, the best thing to do is a minimization of the residuals through a fitting procedure. Since the residual distribution is not parabolic but can be approximated to a parabola in the region near the minimum, I isolate the 300 points nearest to the minimum and I fitted them to a parabola. Finally I take the value of the dispersion of the intrinsic proper motion which corresponds to the minimum of the parabola that best fits the residuals.

I performed this procedure both on the sample of points measured in all the 8 *epochs* and those measured in at least 2, results are shown in figure 27.

The results obtained from the Monte Carlo procedure agree with my results both for the data-set restricted to the points with the highest accuracy and for the largest data-set which includes also stars with larger uncertainties. This sanity-check confirms my results.
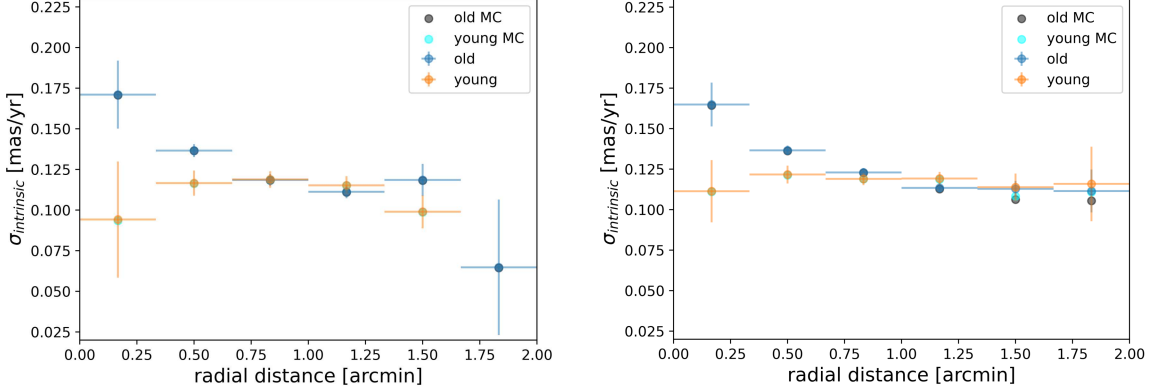
(a) Overlaying of the Monte Carlo simulation results with the original data from the data-set containing stars detected in all the 8 *epochs*

(b) Overlaying of the Monte Carlo simulation results with the original data from the data-set containing stars detected in at least 2 *epochs*

Figure 27: Comparison of the results of the Monte Carlo simulation with the original data on the radial axis. On the left results of the simulation using the data-set containing stars detected in all the 8 *epochs* (figure 27a) while on the right results from the data-set of stars detected in at least 2 *epochs* (figure 27b). Results from the Monte Carlo simulations are assumed to be error-less, the error-bars are referred to the original data and represent respectively the uncertainty on the intrinsic dispersion obtained from the bootstrap method and along the abscissa represent the bin width from which stars were taken.

I can conclude that the results that I obtain agree with those coming from the Monte Carlo simulations and therefore I can trust on them.

A.3   Error propagation on the ratio of velocity-dispersion

To propagate the uncertainties over the ratio I refer to the classical law of propagation that considers the variance of the ratio as the variance of the first variable times the square of the partial derivative of the ratio with respect to the first variable summed with the same quantity computed with respect to the second variable. Considering the ratio operation as $R = \frac{\sigma_{obsP1}}{\sigma_{obsP2}}$ then

$$\sigma_R = \sqrt{\sigma^2_{\sigma_{obsP1}} \left(\frac{\partial R}{\partial \sigma_{obsP1}} \right)^2 + \sigma^2_{\sigma_{obsP2}} \left(\frac{\partial R}{\partial \sigma_{obsP2}} \right)^2} \qquad (8)$$

where $\sigma_{\sigma_{obsP1}}$ and $\sigma_{\sigma_{obsP2}}$ are the standard deviation computed from the bootstrap procedure explained in section 3.2. In principle as $\sigma_{\sigma_{obsP1}}$ I should use the dispersion of the errors

(previously referred to as σ_{err}) but this latter is sensible to the fact that in the outskirts I have just poorly detected stars which causes it to be overestimated. The errors obtained from the bootstrap procedure, even if referred to the intrinsic dispersion and not to the dispersion of the errors, are more robust and strictly connected to the dispersion of the errors.

Exploiting the derivatives the previous equation become:

$$\sigma_R = \frac{1}{\sigma_{obsP2}} \sqrt{\sigma^2_{\sigma_{obsP1}} + R^2 \sigma^2_{\sigma_{obsP2}}} \tag{9}$$

This is the equation used to propagate the uncertainties from the velocity-dispersion distribution to their ratio.

List of Figures

List of Tables

Bibliography

Alfaro-Cuello, M. et al. (Nov. 2019). "A Deep View into the Nucleus of the Sagittarius Dwarf Spheroidal Galaxy with MUSE. I. Data and Stellar Population Characterization". In: ApJ 886.1, 57, p. 57. DOI: `10.3847/1538-4357/ab1b2c`. arXiv: `1909.10529 [astro-ph.GA]`.

Alfaro-Cuello, M. et al. (Mar. 2020). "A Deep View into the Nucleus of the Sagittarius Dwarf Spheroidal Galaxy with MUSE. II. Kinematic Characterization of the Stellar Populations". In: ApJ 892.1, 20, p. 20. DOI: `10.3847/1538-4357/ab77bb`. arXiv: `2002.07814 [astro-ph.GA]`.

Anderson (Jan. 2003). "Astrometry with the Advanced Camera: PSFs and Distortion in the WFC and HRC". In: *HST Calibration Workshop : Hubble after the Installation of the ACS and the NICMOS Cooling System*, p. 13.

Anderson et al. (June 2008). "The Acs Survey of Globular Clusters. V. Generating a Comprehensive Star Catalog for each Cluster". In: AJ 135.6, pp. 2055–2073. DOI: `10.1088/0004-6256/135/6/2055`. arXiv: `0804.2025 [astro-ph]`.

Anderson & King (Oct. 2000). "Toward High-Precision Astrometry with WFPC2. I. Deriving an Accurate Point-Spread Function". In: PASP 112.776, pp. 1360–1382. DOI: `10.1086/316632`. arXiv: `astro-ph/0006325 [astro-ph]`.

Astropy Collaboration et al. (Oct. 2013). "Astropy: A community Python package for astronomy". In: A&A 558, A33, A33. DOI: `10.1051/0004-6361/201322068`. arXiv: `1307.6212 [astro-ph.IM]`.

Astropy Collaboration et al. (Sept. 2018). "The Astropy Project: Building an Open-science Project and Status of the v2.0 Core Package". In: AJ 156.3, 123, p. 123. DOI: `10.3847/1538-3881/aabc4f`. arXiv: `1801.02634 [astro-ph.IM]`.

Bastian, N. et al. (Dec. 2013). "Early disc accretion as the origin of abundance anomalies in globular clusters". In: MNRAS 436.3, pp. 2398–2411. DOI: `10.1093/mnras/stt1745`. arXiv: `1309.3566 [astro-ph.GA]`.

Bekki & Freeman (Dec. 2003). "Formation of ω Centauri from an ancient nucleated dwarf galaxy in the young Galactic disc". In: MNRAS 346.2, pp. L11–L15. DOI: `10.1046/j.1365-2966.2003.07275.x`. arXiv: `astro-ph/0310348 [astro-ph]`.

Bekki & Yong (Jan. 2012). "On the origin of the stellar halo and multiple stellar populations in the globular cluster NGC 1851". In: MNRAS 419.3, pp. 2063–2076. DOI: `10.1111/j.1365-2966.2011.19856.x`. arXiv: `1109.4463 [astro-ph.GA]`.

Bellini, A. et al. (Dec. 2009). "Radial distribution of the multiple stellar populations in ω Centauri". In: A&A 507.3, pp. 1393–1408. DOI: `10.1051/0004-6361/200912757`. arXiv: `0909.4785 [astro-ph.SR]`.

Carretta, E. et al. (Sept. 2010). "Detailed abundances of a large sample of giant stars in M 54 and in the Sagittarius nucleus". In: A&A 520, A95, A95. DOI: `10.1051/0004-6361/201014924`. arXiv: `1006.5866 [astro-ph.GA]`.

Cordero, M. J. et al. (Jan. 2014). "Detailed Abundances for a Large Sample of Giant Stars in the Globular Cluster 47 Tucanae (NGC 104)". In: ApJ 780.1, 94, p. 94. DOI: `10.1088/0004-637X/780/1/94`. arXiv: `1311.1541 [astro-ph.SR]`.

Cordoni, G. et al. (Aug. 2020a). "Gaia and Hubble Unveil the Kinematics of Stellar Populations in the Type II Globular Clusters ω Centauri and M22". In: ApJ 898.2, 147, p. 147. DOI: `10.3847/1538-4357/aba04b`. arXiv: `2006.16355 [astro-ph.SR]`.

Cordoni, G. et al. (Jan. 2020b). "Kinematics of multiple stellar populations in Globular Clusters with Gaia". In: *Star Clusters: From the Milky Way to the Early Universe*. Ed. by Angela Bragaglia, Melvyn Davies, Alison Sills, and Enrico Vesperini. Vol. 351, pp. 281–284. DOI: `10.1017/S1743921319007737`. arXiv: `1908.11692 [astro-ph.SR]`.

Cordoni, G. et al. (Jan. 2020c). "Three-component Kinematics of Multiple Stellar Populations in Globular Clusters with Gaia and VLT". In: ApJ 889.1, 18, p. 18. DOI: `10.3847/1538-4357/ab5aee`. arXiv: `1905.09908 [astro-ph.SR]`.

D'Antona, F. et al. (May 2016). "A single model for the variety of multiple-population formation(s) in globular clusters: a temporal sequence". In: MNRAS 458.2, pp. 2122–2139. DOI: `10.1093/mnras/stw387`. arXiv: `1602.05412 [astro-ph.GA]`.

D'Ercole, Annibale et al. (Sept. 2010). "Abundance patterns of multiple populations in globular clusters: a chemical evolution model based on yields from AGB ejecta". In: MNRAS 407.2, pp. 854–869. DOI: `10.1111/j.1365-2966.2010.16996.x`. arXiv: `1005.1892 [astro-ph.GA]`.

de Mink, S. E., O. R. Pols, N. Langer, and R. G. Izzard (Nov. 2009). "Massive binaries as the source of abundance anomalies in globular clusters". In: A&A 507.1, pp. L1–L4. DOI: `10.1051/0004-6361/200913205`. arXiv: `0910.1086 [astro-ph.SR]`.

Decressin, T. (Dec. 2010). "Multiple populations in globular clusters: a theoretical point of view". In: *SF2A-2010: Proceedings of the Annual meeting of the French Society of Astronomy and Astrophysics*. Ed. by S. Boissier, M. Heydari-Malayeri, R. Samadi, and D. Valls-Gabaud, p. 345.

Decressin, T. et al. (Mar. 2007). "Fast rotating massive stars and the origin of the abundance patterns in galactic globular clusters". In: A&A 464.3, pp. 1029–1044. DOI: `10.1051/0004-6361:20066013`. arXiv: `astro-ph/0611379 [astro-ph]`.

Denissenkov, P. A. and F. D. A. Hartwick (Jan. 2014). "Supermassive stars as a source of abundance anomalies of proton-capture elements in globular clusters". In: MNRAS 437.1, pp. L21–L25. DOI: `10.1093/mnrasl/slt133`. arXiv: `1305.5975 [astro-ph.SR]`.

Dondoglio, E. et al. (Jan. 2021). "Multiple Stellar Populations along the Red Horizontal Branch and Red Clump of Globular Clusters". In: ApJ 906.2, 76, p. 76. DOI: `10.3847/1538-4357/abc882`. arXiv: `2011.03283 [astro-ph.GA]`.

Gieles, Mark et al. (Aug. 2018). "Concurrent formation of supermassive stars and globular clusters: implications for early self-enrichment". In: MNRAS 478.2, pp. 2461–2479. DOI: `10.1093/mnras/sty1059`. arXiv: `1804.04682 [astro-ph.GA]`.

González-Núñez, J. et al. (Mar. 2021). *Gaia EDR3 documentation Chapter 12: ESA Gaia Archive*. Gaia EDR3 documentation.

Harris, William E. (Oct. 1996). "A Catalog of Parameters for Globular Clusters in the Milky Way". In: AJ 112, p. 1487. DOI: `10.1086/118116`.

Hénault-Brunet, V., M. Gieles, O. Agertz, and J. I. Read (June 2015). "Multiple populations in globular clusters: the distinct kinematic imprints of different formation scenarios". In: MNRAS 450.2, pp. 1164–1198. DOI: `10.1093/mnras/stv675`. arXiv: `1503.07532 [astro-ph.GA]`.

Ibata, R. et al. (July 2009). "Density and Kinematic Cusps in M54 at the Heart of the Sagittarius Dwarf Galaxy: Evidence for A 10^4 M $_{sun}$ Black Hole?" In: ApJ 699.2, pp. L169–L173. DOI: `10.1088/0004-637X/699/2/L169`. arXiv: `0906.4894 [astro-ph.GA]`.

Ibata, R. A., G. Gilmore, and M. J. Irwin (July 1994). "A dwarf satellite galaxy in Sagittarius". In: Nature 370.6486, pp. 194–196. DOI: `10.1038/370194a0`.

Ibata, R. A., Michael Irwin, Geraint F. Lewis, and Andrea Stolte (Feb. 2001). "Galactic Halo Substructure in the Sloan Digital Sky Survey: The Ancient Tidal Stream from the Sagittarius Dwarf Galaxy". In: ApJ 547.2, pp. L133–L136. DOI: `10.1086/318894`. arXiv: `astro-ph/0004255 [astro-ph]`.

Ibata, R. A. et al. (Apr. 2019). "Identification of the long stellar stream of the prototypical massive globular cluster ω Centauri". In: *Nature Astronomy* 3, pp. 667–672. DOI: `10.1038/s41550-019-0751-x`. arXiv: `1902.09544 [astro-ph.GA]`.

Kraft, R. P. (Jan. 1979). "On the nonhomogeneity of metal abundances in stars of globular clusters and satellite subsystems of the Galaxy." In: ARA&A 17, pp. 309–343. DOI: `10.1146/annurev.aa.17.090179.001521`.

Krause, M. et al. (Apr. 2013). "Superbubble dynamics in globular cluster infancy. II. Consequences for secondary star formation in the context of self-enrichment via fast-rotating massive stars". In: A&A 552, A121, A121. DOI: `10.1051/0004-6361/201220694`. arXiv: `1302.2494 [astro-ph.GA]`.

Lagioia, Edoardo P. et al. (Nov. 2019). "The Role of Cluster Mass in the Multiple Populations of Galactic and Extragalactic Globular Clusters". In: AJ 158.5, 202, p. 202. DOI: `10.3847/1538-3881/ab45f2`. arXiv: `1909.08439 [astro-ph.SR]`.

Lauer, Tod R. (Nov. 1999). "The Photometry of Undersampled Point-Spread Functions". In: PASP 111.765, pp. 1434–1443. DOI: `10.1086/316460`. arXiv: `astro-ph/9907100 [astro-ph]`.

Marino, A. F. et al. (Aug. 2014). "The halo+cluster system of the Galactic globular cluster NGC 1851". In: MNRAS 442.4, pp. 3044–3064. DOI: `10.1093/mnras/stu1099`. arXiv: `1406.0944 [astro-ph.SR]`.

Marino, A. F. et al. (June 2015). "Iron and s-elements abundance variations in NGC 5286: comparison with 'anomalous' globular clusters and Milky Way satellites". In: MNRAS 450.1, pp. 815–845. DOI: `10.1093/mnras/stv420`. arXiv: `1502.07438 [astro-ph.SR]`.

Marino, A. F. et al. (Aug. 2019). "The Hubble Space Telescope UV Legacy Survey of Galactic Globular Clusters - XIX. A chemical tagging of the multiple stellar populations over the chromosome maps". In: MNRAS 487.3, pp. 3815–3844. DOI: `10.1093/mnras/stz1415`. arXiv: `1904.05180 [astro-ph.SR]`.

Marino, A. F. et al. (June 2021). "Spectroscopy and photometry of the least-massive Type-II globular clusters: NGC1261 AND NGC6934". In: *arXiv e-prints*, arXiv:2106.15978, arXiv:2106.15978. arXiv: 2106.15978 [astro-ph.SR].

Milone, A. P. (Aug. 2016). "Multiple populations in the Sagittarius nuclear cluster M 54 and in other anomalous globular clusters". In: *The General Assembly of Galaxy Halos: Structure, Origin and Evolution*. Ed. by A. Bragaglia, M. Arnaboldi, M. Rejkuba, and D. Romano. Vol. 317, pp. 170–175. DOI: 10.1017/S1743921315008467. arXiv: 1510.02578 [astro-ph.SR].

Milone, A. P., A. F. Marino, A. Mastrobuono-Battisti, and E. P. Lagioia (Oct. 2018a). "Gaia unveils the kinematics of multiple stellar populations in 47 Tucanae". In: MNRAS 479.4, pp. 5005–5011. DOI: 10.1093/mnras/sty1873. arXiv: 1807.03511 [astro-ph.SR].

Milone, A. P. et al. (Sept. 2009). "The radial distribution of the two stellar populations in NGC 1851". In: A&A 503.3, pp. 755–764. DOI: 10.1051/0004-6361/200912256. arXiv: 0906.1779 [astro-ph.SR].

Milone, A. P. et al. (Apr. 2012). "The ACS survey of Galactic globular clusters. XII. Photometric binaries along the main sequence". In: A&A 540, A16, A16. DOI: 10.1051/0004-6361/201016384. arXiv: 1111.0552 [astro-ph.SR].

Milone, A. P. et al. (July 2015). "The Hubble Space Telescope UV Legacy Survey of Galactic Globular Clusters. III. A Quintuple Stellar Population in NGC 2808". In: ApJ 808.1, 51, p. 51. DOI: 10.1088/0004-637X/808/1/51. arXiv: 1505.05934 [astro-ph.SR].

Milone, A. P. et al. (Jan. 2017). "The Hubble Space Telescope UV Legacy Survey of Galactic globular clusters - IX. The Atlas of multiple stellar populations". In: MNRAS 464.3, pp. 3636–3656. DOI: 10.1093/mnras/stw2531. arXiv: 1610.00451 [astro-ph.SR].

Milone, A. P. et al. (June 2018b). "Multiple stellar populations in Magellanic Cloud clusters - VI. A survey of multiple sequences and Be stars in young clusters". In: MNRAS 477.2, pp. 2640–2663. DOI: 10.1093/mnras/sty661. arXiv: 1802.10538 [astro-ph.SR].

Milone, A. P. et al. (Dec. 2018c). "The Hubble Space Telescope UV legacy survey of galactic globular clusters - XVI. The helium abundance of multiple populations". In: MNRAS 481.4, pp. 5098–5122. DOI: 10.1093/mnras/sty2573. arXiv: 1809.05006 [astro-ph.SR].

Milone, A. P. et al. (Apr. 2019). "The HST Large Programme on NGC 6752 - II. Multiple populations at the bottom of the main sequence probed in NIR". In: MNRAS 484.3, pp. 4046–4053. DOI: 10.1093/mnras/stz277. arXiv: 1901.07230 [astro-ph.SR].

Milone, A. P. et al. (Jan. 2020). "Multiple populations in globular clusters and their parent galaxies". In: MNRAS 491.1, pp. 515–531. DOI: 10.1093/mnras/stz2999. arXiv: 1910.09683 [astro-ph.GA].

Minniti, D. et al. (June 2021). "Eight more low luminosity globular clusters in the Sagittarius dwarf galaxy". In: A&A 650, L12, p. L12. DOI: 10.1051/0004-6361/202140714. arXiv: 2106.03605 [astro-ph.GA].

Monaco, L., M. Bellazzini, F. R. Ferraro, and E. Pancino (Feb. 2005). "The central density cusp of the Sagittarius dwarf spheroidal galaxy". In: MNRAS 356.4, pp. 1396–1402. DOI: `10.1111/j.1365-2966.2004.08579.x`. arXiv: `astro-ph/0411107 [astro-ph]`.

Noyola, Eva, K. Gebhardt, and M. Bergmann (Dec. 2009). "Internal Kinematics For The Globular Cluster M54". In: *American Astronomical Society Meeting Abstracts #213*. Vol. 213. American Astronomical Society Meeting Abstracts, p. 605.08.

Olszewski, Edward W. et al. (Dec. 2009). "A 500 Parsec Halo Surrounding the Galactic Globular NGC 1851". In: AJ 138.6, pp. 1570–1576. DOI: `10.1088/0004-6256/138/6/1570`. arXiv: `0909.1755 [astro-ph.GA]`.

Plummer, H. C. (Mar. 1911). "On the problem of distribution in globular star clusters". In: MNRAS 71, pp. 460–470. DOI: `10.1093/mnras/71.5.460`.

Sarajedini, Alta and Andrew C. Layden (Mar. 1995). "A Photometric Study of the Globular Cluster M54 and the Sagittarius Dwarf Galaxy: Evidence for Three Distinct Populations". In: AJ 109, p. 1086. DOI: `10.1086/117343`.

Siegel, Michael H. et al. (Sept. 2007). "The ACS Survey of Galactic Globular Clusters: M54 and Young Populations in the Sagittarius Dwarf Spheroidal Galaxy". In: ApJ 667.1, pp. L57–L60. DOI: `10.1086/522003`. arXiv: `0708.0027 [astro-ph]`.

Sollima, A. et al. (Jan. 2007). "Deep FORS1 Observations of the Double Main Sequence of ω Centauri". In: ApJ 654.2, pp. 915–922. DOI: `10.1086/509711`. arXiv: `astro-ph/0609650 [astro-ph]`.

Stetson, Peter B. (June 2005). "Homogeneous Photometry. IV. On the Standard Sequence in the Globular Cluster NGC 2419". In: PASP 117.832, pp. 563–588. DOI: `10.1086/430281`. arXiv: `astro-ph/0503393 [astro-ph]`.

van Leeuwen, F. et al. (Mar. 2021). *Gaia EDR3 documentation*. Gaia EDR3 documentation.

Ventura, Paolo, Francesca D'Antona, Italo Mazzitelli, and Raffaele Gratton (Mar. 2001). "Predictions for Self-Pollution in Globular Cluster Stars". In: ApJ 550.1, pp. L65–L69. DOI: `10.1086/319496`. arXiv: `astro-ph/0103337 [astro-ph]`.

Virtanen, Pauli et al. (2020). "SciPy 1.0: Fundamental Algorithms for Scientific Computing in Python". In: *Nature Methods* 17, pp. 261–272. DOI: `10.1038/s41592-019-0686-2`.

Zennaro, M. et al. (Aug. 2019). "Four stellar populations and extreme helium variation in the massive outer-halo globular cluster NGC 2419". In: MNRAS 487.3, pp. 3239–3251. DOI: `10.1093/mnras/stz1477`. arXiv: `1902.02178 [astro-ph.SR]`.